5-2024

Electrokinetic particle trapping performance of conductive nanofiber mats in microfluidic wells.

Jacob Hunter West
University of Louisville

Recommended Citation

ELECTROKINETIC PARTICLE TRAPPING PERFORMANCE OF CONDUCTIVE

NANOFIBER MATS IN MICROFLUIDIC WELLS

By

Jacob Hunter West

B.S., University of Louisville, 2023

A Thesis

Submitted to the Faculty of the

J.B. Speed School of Engineering of the University of Louisville

In Partial Fulfillment of the Requirements for the Degree of

Master of Science

in Mechanical Engineering

Department of Mechanical Engineering

University of Louisville

Louisville, KY

May 2024

ELECTROKINETIC PARTICLE TRAPPING PERFORMANCE OF CONDUCTIVE

NANOFIBER MATS IN MICROFLUIDIC WELLS

By

Jacob Hunter West

B.S., University of Louisville, 2023

A Thesis Approved on

April 17, 2024

by the following Thesis Committee:

_____

Thesis Chair: Stuart J. Williams

_____

Committee member: Ellen G. Brehob

_____

Committee member: Robert W. Cohn

ACKNOWLEDGEMENTS

ABSTRACT

ELECTROKINETIC PARTICLE TRAPPING PERFORMANCE OF CONDUCTIVE

NANOFIBER MATS IN MICROFLUIDIC WELLS

Jacob Hunter West

April 17, 2024

The frequency dependence of electrokinetic particle trapping using large-area ($>mm^2$) conductive carbon nanofiber (CNF) mat electrodes is investigated. The fibers provide nanoscale geometric features for the generation of high electric field gradients, which is necessary for particle trapping via dielectrophoresis (DEP). A device was fabricated with an array of microfluidic wells for repeated experiments; each well included a CNF mat electrode opposing an aluminum electrode. Fluorescent microspheres (1 μm) were trapped at various electric field frequencies between 30 kHz – 1 MHz. Digital images of each well were analyzed to quantify particle trapping. DEP trapping by the CNF mats was greater at all tested frequencies than that of the control of no applied field, and the greatest trapping was observed at a frequency of 600 kHz, where electrothermal (ET) flow is more significantly weakened than DEP. This result indicates the contribution to particle trapping by ET flow is not exclusively positive.

TABLE OF CONTENTS

LIST OF FIGURES

CHAPTER I

INTRODUCTION

Motivation

The primary motivation of this study is the need to develop techniques for high throughput trapping and sorting of nanoparticles. Mechanical filtration techniques can efficiently filter suspended particles on the length scale of a few microns as seen with commonly available HVAC filters [1], but nanoscale particulates are less easily captured by traditional filtration schemes [2].

Sub-micron particle trapping is of special significance because of relevant applications in healthcare and multiple industrial sectors [3]. The lack of high throughput nanoparticle trapping techniques poses a challenge when the collection and/or sorting of some biological particles is of interest. Viruses, exosomes, protein aggregates, and bacteria all occupy portions of the sub-micron regime [4], meaning trapping such biological species for analysis and characterization is difficult to accomplish at high throughput. Biofiltration is a growing market, valued at over $2B globally in 2022 [5]. Additionally, as discussed by Salafi et al. [3], nanoparticles have other applications in industries such as photovoltaics and supercapacitors, and the separation of nanoparticles from industrial waste could help curtail health and environmental safety concerns. Therefore, the development of high throughput nanoparticle filtration techniques has the potential for broad societal impact.

Electrokinetic techniques are methods (used primarily for microfluidic applications) in which, broadly speaking, electric fields applied to a fluid medium induce the motion of fluids and/or particles through their action on charge-carrying entities [6]. Electrokinetic techniques are commonly used for the manipulation and sorting of nanoparticles, but the throughput of such methods is often very low (~nL/min fluid processing rates) [3]. These techniques are often dependent upon the dielectric properties of the particle species and/or the suspending fluid medium as well as the parameters of the applied electric field [7].

Electrokinetic effects can be used for a variety of goals related to particle manipulation. Electrode configurations and other factors can be designed to pattern particles near sharp conductive [8] or insulative [9] features, trap particles within pores [10], or focus particles at prescribed locations within the bulk fluid medium [11], to name only a few of the patterning/trapping possibilities. Separation and sorting of particles by size or properties can also be accomplished using electrokinetic systems [12]. For the purposes of this study, which utilizes mats of electrically conductive nanofibers as electrodes, the phrase "particle trapping" refers to the use of electrokinetic effects to attract a particle and cause it to become adhered to the surface of the electrode. Furthermore, comparison of "trapping performance" between different electrode arrangements or electric field frequencies refers to a comparison of the number of particles which are successfully trapped, as determined by some quantifiable metric.

This study builds upon previous work in which conductive nanofiber (CNF) mat electrodes were used in a novel nanoparticle trapping approach using a well-studied

electrokinetic phenomenon known as dielectrophoresis (DEP) [13]. Traditional DEP particle trapping methods are hindered by low throughput as with many electrokinetic trapping techniques, but the use of CNF mat electrodes might enable DEP particle trapping at much greater throughput (~mL/min). Although preliminary results showed the CNF mats are capable of trapping nanoparticles using DEP, the extent of the mats' trapping performance and the interaction of other electrokinetic phenomena was not fully understood. Therefore, the desired outcome of the study was twofold: first, to have a repeatable, unsophisticated experimental procedure by which electrokinetic CNF electrodes could be tested and particle trapping quantified; and second, to better understand the interaction of DEP and other electrokinetic effects so that particle, fluid medium, and electric field parameters could be chosen for the optimization of trapping performance in subsequent applications.

The following discussions concern additional background which motivated this study. First, an overview of the limitations of mechanical filtration will be discussed. Next is an introduction to electrokinetic techniques, which have been widely utilized for particle trapping but traditionally suffer from throughput limitations. This is followed by a discussion of electrospinning, a low-cost fabrication technique by which nanofiber mats can be produced. Last is an overview of work preceding this study in which nanofiber mats created via electrospinning were made electrically conductive and used as electrodes for electrokinetic trapping of nanoparticles. These electrodes have the potential to improve electrokinetic trapping throughput, and this study was an investigation of the electric field frequency-dependence of their electrokinetic particle trapping performance.

Mechanical filtration

There are several common methods of mechanical particle filtration (e.g.
sedimentation, impaction, interception, Brownian diffusion), each with collection
efficiencies dependent on particle size. For mechanical filtration schemes (e.g. fibrous
filters), the combination of these mechanisms produces an overall collection efficiency
for a given filter, flowrate, and particle species. Visualizations of these mechanisms are
shown in Figure 1A. As particle size decreases, the effectiveness of interception,
impaction, and settling decrease due to reduction of particle inertial effects, while that of
diffusion increases due to the increased Brownian motion. Therefore, such filtration
schemes typically have high collection efficiency for sufficiently large or small particles,
with a local minimum in combined efficiency occurring in the intermediate range. These
trends are shown in Figure 1B.
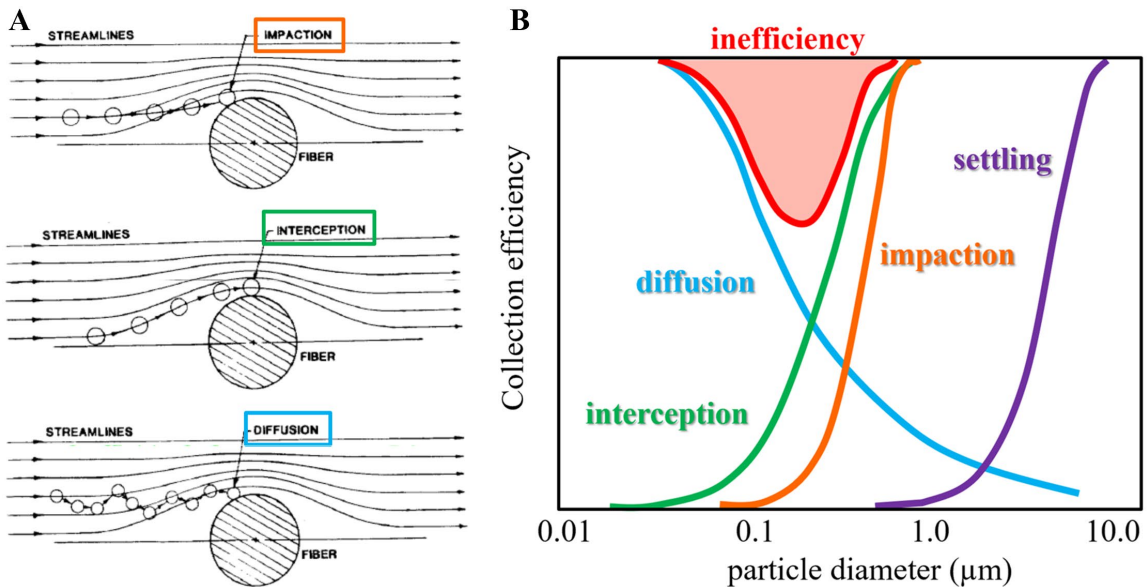
Figure 1. (A): Visual representations of mechanical particle filtration mechanisms
utilized in fibrous filters. (B): Graph showing trends of filtration efficiency plotted
against particle size for fibrous filters. Note that the MPPS is different for each filtration
scheme, but general trends are valid for many filter setups with both gaseous and liquid
media. Adapted from [2].

For a given filtration scheme, the particle size at which the overall efficiency is at a minimum is known as the "most penetrating particle size" or MPPS [14]. While the MPPS varies based on the filter and fluid flowrate, this size is generally in the range of 100 – 200 nm for most non-charged filter media [15]. It is possible to trap sub-micron particles using mechanical methods, but this capacity comes with the tradeoff of greater energy input for a given yield, and furthermore, mechanical filtration is limited in its selectivity of trapping with respect to particle properties other than size and/or density. Therefore, in order to achieve high-throughput nanoparticle filtration, mechanical separation methods are insufficient, and other techniques must be utilized.

Electrokinetic techniques

One approach which, unlike mechanical filtration, is well suited for manipulation and trapping of nanoparticles is the use of electrokinetic techniques. Electrokinetic methods have been widely utilized for particle trapping, and they are advantageous in that they can be easily implemented into microfluidic systems using well established electrode microfabrication processes [6]. Electrokinetic phenomena utilize the forces exerted by externally applied electric fields on dissolved ions and suspended charge carriers to induce motion of particles or the fluid medium [6]. Electric fields scale inversely with length scale, and many electrokinetic techniques involve surface forces, making these methods especially well-suited for microfluidic applications [6]. Because electrokinetic phenomena are dependent upon the dielectric properties of the fluid medium and/or particles, such methods are often used for selectively addressing specific particles within a fluid medium by size, chemical species, or other properties (e.g. alive versus dead in the case of cells) [16,17]. The ability to selectively target a given particle

size, species, etc. from among a polydisperse suspension is advantageous for medical and other biological applications [18], and in the case of some techniques (e.g. dielectrophoresis), the particles need not even carry a net charge to be subject to trapping [19]. Despite these advantages, electrokinetic techniques suffer from very low throughput as implemented traditionally [3].

Dielectrophoresis is an electrokinetic technique frequently utilized for trapping, sorting, and characterizing both biological [18,20] and non-biological [12] particles at the micro- and nanoscale. The DEP force is induced when polarizable particles are exposed to high spatial electric field gradients [19]. These high field gradients are often created using electrodes with sharp geometries (e.g., electrokinetic nanoprobes [21], nanogap electrodes [22], castellated planar electrodes [23], micro- and nanopores [9,24,25], etc.). DEP systems with nanoscale electrode geometries often require specialized and expensive microfabrication techniques such as electron beam lithography [26] or plasma-enhanced chemical vapor deposition [27]. Furthermore, specialized nanoscale electrode fabrication, in general, is not amenable to large surface area features with consistent high spatial field gradients throughout. As a result, most DEP systems suffer from limited throughput capability (nL/min) [3,12]. This limitation is made worse for smaller particle sizes, as the DEP force scales with particle volume.

One of the techniques developed to address the throughput limitation is the use of 3D porous media to create insulative DEP (iDEP) trapping systems [28,29]. Despite the improvements of throughput for microparticle trapping (mL/min), the field gradients necessary to efficiently trap nanoparticles at such flowrates cannot be generated feasibly by these porous media systems because the smallest features are typically on the

microscale. To achieve high throughput trapping of nanoparticles, having the ability to

create a large number of conductive nanoscale features (without the need to utilize

sophisticated and expensive fabrication techniques) would be beneficial.

<div align="center">Electrospinning</div>

Electrospinning is a technique that can produce nanoscale features across

macroscale areas ($>mm^2$) at much lower cost than techniques traditionally used for

nanoscale electrode fabrication in electrokinetic systems. Electrospinning is a method by

which nonwoven polymer nanofiber mats can be fabricated without the use of cleanroom

equipment. While techniques vary, most electrospinning setups consist of a few

fundamental components: a syringe pump, a metal-tipped syringe containing a polymer

solution, and metal collector plate, and DC high-voltage generator [30]. An image of the

electrospinning setup used in this study can be seen in Figure 2.
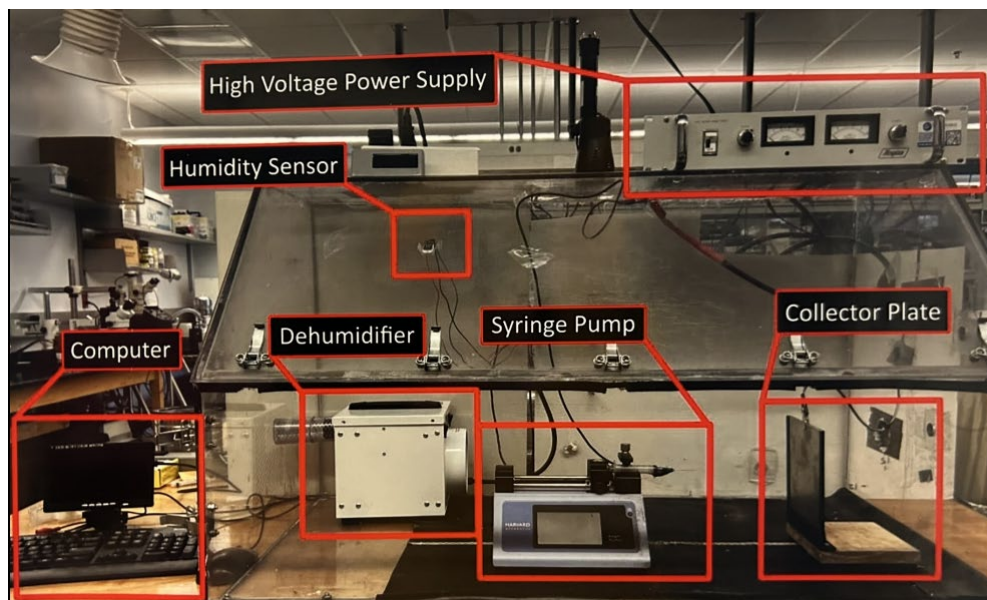
Figure 2. Electrospinning setup used for fabrication of nanofiber mats used in this study
and proof-of-concept study with major components labeled.

To perform electrospinning, a high DC voltage (~kV) is applied between the

syringe needle and collector, and the polymer solution is pumped through the syringe at a

low flowrate (~mL/hr) [30]. A droplet of the polymer solution forms at the syringe tip, where surface tension and electrostatic forces are in opposition; when surface tension is overcome, the polymer solution forms a so-called Taylor cone at the syringe tip, and a high aspect ratio fiber jets from the cone tip toward the metal collector [31]. The solvent evaporates while traversing the gap between the syringe tip and collector plate and a nanofiber (often between 100 – 500 nm in diameter) is subsequently deposited on the collector [31]. The unstable nature of this process results in irregular deposition of the nanofiber on the surface of the collector.

Characteristics of the deposited nanofiber mat (fiber diameter, mat porosity, etc.) can be varied through control of the setup parameters such as applied DC potential, solution flowrate, and distance between syringe and collector [32]. The use of a planar collector results in a random deposition of nanofibers into a nonwoven mat. To better control this deposition process, specially designed collectors (e.g. rotating drums, revolving conveyers, post-shaped electrode pairs, microfabricated patterned electrodes, etc.) can be used to generate patterned mats with control of the macroscale mat shape and/or uni- or multi-axial alignment of fibers [32]. Techniques using multiple adjacent or coaxial needles have also been developed for the use of multiple materials in one electrospinning operation [30]. Other parameters such as temperature of the polymer solution and air as well as the relative humidity can also affect the electrospun nanofiber mats' porosity, fiber size, and morphology [30,31]. Furthermore, many variations on the fundamental electrospinning setup described herein have been developed to control the resulting fiber mats; such setups are described in greater detail elsewhere [30].

The use of electrospun electrically conductive nanofibers has previously been explored for use in supercapacitors for their high surface area, advantageous mechanical properties, and high capacitance [33]. However, the use of conductive nanofibers as electrodes for electrokinetic particle trapping has been previously unexplored. The creation of macroscale electrodes with nanoscale conductive features using electrospinning has the potential to overcome the throughput limitation of traditional electrokinetic trapping approaches, which traditionally require sophisticated micro- and nanofabrication processes.

Previous work

Previous work demonstrated a method by which electrospinning was used to fabricate macroscale ($>$cm^2) mats of conductive carbon nanofibers (CNF) which were then used as electrodes for electrokinetic particle trapping. The fabrication methods and proof-of-concept experiments discussed herein are further described by Mondal et al. [13]. Much of the following discussion in this section is reproduced from [13] with permission from the Royal Society of Chemistry.

The nanofibers used in this study were electrospun from a dimethylformamide solution of polyacrylonitrile (PAN) doped with carbon nanotubes to increase electrical conductivity and phthalic acid to improve mechanical properties. The solution was electrospun using an applied potential of 12 kV DC at a flowrate of 0.5 mL/hr. The PAN mat was subsequently pyrolyzed in a nitrogen atmosphere to carbonize the fibers. A flowchart summarizing the fabrication steps used to create the conductive nanofibers is shown in Figure 3.
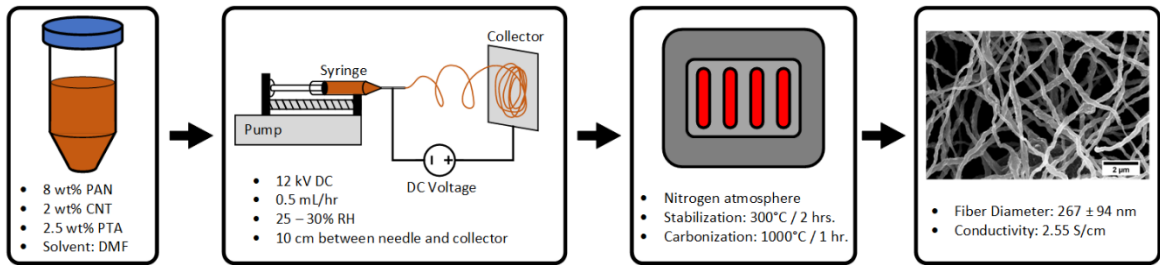
Figure 3. Flow chart summarizing the fabrication steps for electrospun conductive nanofiber mats. A PAN solution with dopants is electrospun and then pyrolyzed to create carbon nanofibers. Reproduced from [13] with permission from the Royal Society of Chemistry.

Conductive nanofiber mats created using the process described in Figure 3 were used in proof-of-concept experiments to demonstrate their potential for use as electrodes in DEP trapping systems. A strip of a CNF mat presoaked with DI water + 0.1% Tween 20, a common surfactant, was dipped into a reservoir containing a suspension of fluorescent polystyrene particles on an indium tin oxide (ITO, an optically transparent and electrically conductive material) coated glass slide. No particle trapping occurred at this point; moreover, the presence of the mat in absence of an electric field did not appear to cause any particle motion. An AC potential was applied between the CNF mat and the ITO slide, and particle motion was observed from below through the glass slide using an inverted microscope. Both attraction (positive DEP) and repulsion (negative DEP) from the CNF mats were observed during these experiments when the electric field was active; additionally, vortical fluid motion characteristic of electrothermal (ET) flow was also observed. Figure 4 shows a schematic of the experimental setup as well as images of CNF mat samples within the particle suspension during the experiments both immediately before the application of an electric field and after the electric field had been applied for approximately 140 seconds. Particles as small as 20 nm were successfully

trapped during these experiments. It was observed that most trapped particles remained in contact with the CNF mat even after removal of the field.
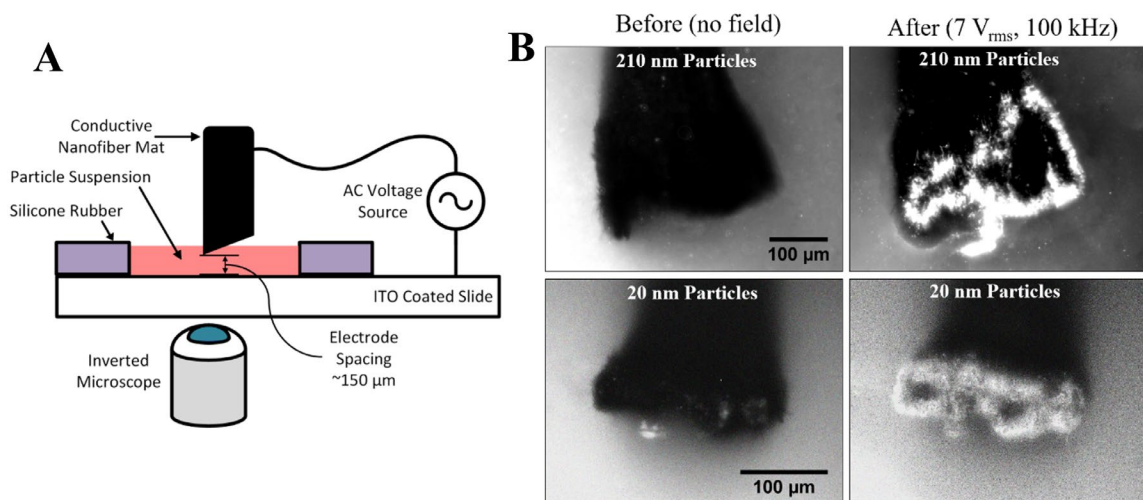
Figure 4. (A): Schematic of proof-of-concept experimental setup for demonstration of DEP trapping using CNF mats. (B): Images of CNF mat samples captured during experiments both before the application of electric fields and after approximately 140 seconds of electric field application showing successful trapping of nanoparticles (210 nm and 20 nm). Adapted from [13] with permission from the Royal Society of Chemistry.

Previous experiments demonstrated the frequency dependence of both DEP and other electrohydrodynamic (EHD) effects, but quantifying particle trapping as a function of frequency and voltage was not attempted. Furthermore, the impact of EHD phenomena such as electrothermal (ET) flow and AC electroosmosis (ACEO) on particle trapping was not studied. In order to use the CNF mats for high-throughput DEP systems, these effects must first be understood.

For this study, a microfluidic well device was fabricated without using traditional micro/nano fabrication techniques that incorporated a CNF mat as an electrode for repeatable particle trapping trials across a broad range of electric field frequencies. The frequency-dependence of particle trapping performance was investigated to gain insight into the relative benefit or detriment of EHD phenomena. Furthermore, having a device

for characterization of electrokinetic trapping performance that could be constructed without the use of expensive microfabrication techniques would enable future comparison of trapping performance between CNF mats of different morphologies, materials, etc. at low cost. Particle trapping experiments performed with these devices could inform the selection of both electric field frequencies and CNF mat morphologies for throughput optimization in electrokinetic particle filtration applications.

CHAPTER II

THEORY

Dielectrophoresis

Dielectrophoresis is an electrokinetic phenomenon commonly utilized for particle

trapping. When a neutrally charged, polarizable particle is subjected to a non-uniform

electric field, a dipole moment is induced on the particle [34]. If the electric field is

sufficiently non-uniform (i.e. if the spatial gradient is sufficiently great), the effect of the

electric field in polarizing the particle will be asymmetric. The asymmetric field effect

on this dipole moment results in a net force either toward (positive DEP) or away from

(negative DEP) the increasing field strength depending on the dielectric properties of

both the particle and the fluid medium [35]. If the particle is more polarizable than the

fluid medium, positive DEP will occur, whereas negative DEP occurs in the opposite case

[34]. Qualitative schematics of DEP acting on suspended particles within different

electric field configurations are shown in Figure 5.

The direction and frequency dependence of the DEP force are determined by the

Clausius-Mossotti factor, which can be calculated using [19]

$$CM(\omega) = \frac{\tilde{\varepsilon}_p - \tilde{\varepsilon}_m}{\tilde{\varepsilon}_p + 2\tilde{\varepsilon}_m} \text{ ,where } \tilde{\varepsilon} = \varepsilon - j\frac{\sigma}{\omega} \tag{1}$$

where $\tilde{\varepsilon}$ is the complex permittivity of the particle (subscript p) and fluid medium (subscript m), ε is absolute permittivity, σ is electrical conductivity, ω is angular frequency ($\omega = 2\pi f$), and j is $\sqrt{-1}$.
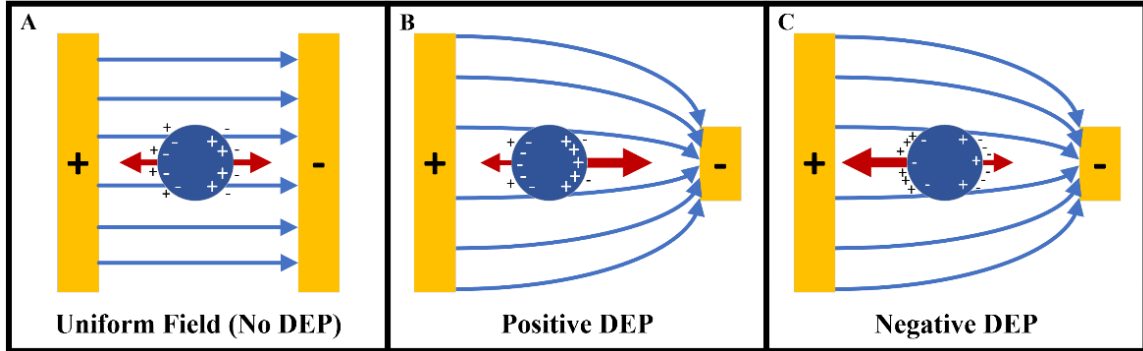
Figure 5. Qualitative schematics of particles in different electric field configurations. (A): Uniform field in which particle experiences no net force. (B): Non-uniform field in which particle is more polarizable than medium and thus experiences a net force toward the areas of greater field strength (positive DEP). (C): Non-uniform field in which particle is less polarizable than medium and thus experiences a net force toward the areas of lower field strength (negative DEP).

As can be seen from Eq. 1, the dielectrophoretic force is a function of the particle dielectric properties, which themselves can be affected by particle-fluid interfacial phenomena. A solid surface within a fluid medium containing dissolved charge carriers will often obtain a surface charge through electrochemical interactions with the fluid. The charged surface will then attract oppositely charged ions from the liquid; the dissolved charges form both a tightly bound layer at the solid-liquid interface, known as the Stern or compact layer, and a more loosely organized layer of more mobile ions known as the Debye or diffuse layer [36]. Together, the compact and diffuse layers are known as the electric double layer (EDL). As particle diameter decreases to approach the thickness of the EDL, the effect of ion mobility in the double layer introduces a surface conductance K_s that can become significant relative to bulk conductivity σ_{bulk}.

Therefore, the total conductivity of a spherical particle can be calculated as the sum of bulk and surface conductivities using [19]

$$\sigma_p = \sigma_{bulk} + \frac{2K_s}{a} \tag{2}$$

where a is particle radius.

Assuming particle homogeneity, the time-averaged magnitude of the DEP force can be calculated by [19]

$$F_{DEP} = 2\pi\tilde{\varepsilon}_m a^3 Re[CM]\nabla|E|^2 \tag{3}$$

where $Re[CM]$ is the real component of the Clausius-Mossotti factor as defined by Eq. 1 and $\nabla|E|^2$ is the gradient of the square of electric field magnitude. It can be seen from (3) that the DEP force is proportional to particle volume, and therefore the trapping force decays rapidly as particle size is reduced. It can also be seen that the DEP force can be increased through high electric field gradients.

<center>Electrohydrodynamics</center>

During both previous experiments [13] and those described herein, electrohydrodynamic (EHD) fluid flows were observed. Electrohydrodynamic flows, broadly speaking, are phenomena which arise through the interaction of electric fields with fluids. Understanding the contribution of these effects to particle trapping was part of the motivation of this study. It was previously assumed that EHD flows augmented DEP trapping in the CNF mats, but further experimental and numerical investigation is required to understand how the combination of EHD phenomena affect trapping. Specifically, electrothermal (ET) hydrodynamics and AC electroosmosis (ACEO) are of concern.

Joule heating is the process of heat generation by electric current passing through a conductor. In a non-uniform electric field, current density, and thus Joule heating, will be similarly non-uniform. The non-uniform heating will induce temperature gradients within the fluid and subsequently gradients in temperature-dependent dielectric properties ε and σ [37]. The non-uniform electric field causes an electric force on free charges within the fluid that causes them to move, and shear stress on the fluid from this motion subsequently induces flow [37]. The primary direction of induced fluid motion in the case of only internal Joule heating will be from locations of strong electric field (high heating) toward areas of weaker field (less heating) [37]. It is noted that non-uniform fluid heating can be caused by an external source (e.g. an incident laser); in such cases, ET flow would occur even in a uniform electric field. However, such external heat sources were avoided in the described experiments.

The maximum ET flow velocity depends on field voltage and fluid properties as given by [35]

$$v_{ET,max} \propto M \frac{\varepsilon_m \sigma_m V^4}{k_m \mu} \tag{4}$$

where V is field voltage, k_m is fluid thermal conductivity, and μ is fluid dynamic viscosity. In Eq. 4, M is a dimensionless factor that is a function of temperature T as well as σ, ε, $\frac{\partial \sigma}{\partial T}$, $\frac{\partial \varepsilon}{\partial T}$, and ω [35]. The frequency-dependence of electrothermal flow magnitude comes from this term, which accounts for the transition between the dominance of conductivity and permittivity. From Eq. 4 and the expression for M, a relaxation frequency can be calculated at which the ET flow is negligible. For the experiments described, the ET flow decays as frequency increases. Importantly, the ET flow velocity

is a function of fluid medium conductivity σ_m, meaning motion increases with fluid conductivity. Therefore, consideration of ET flow is especially relevant in cases of electrokinetic systems using high-conductivity biofluids such as blood [37].

AC electroosmosis is an EHD phenomenon causing fluid flow due to fluid-electrode interfacial interaction. As discussed previously, an electrically charged surface within a fluid medium containing dissolved charge carriers will attract opposite charges and form an electric double layer. The electric field then exerts a force on the charges contained in the EDL causing them to move; movement of the surrounding fluid medium is subsequently generated through viscous effects [38]. This induced fluid motion occurs in the direction of the tangential component of the electric field [39]. This phenomenon is also frequency dependent. At low AC frequencies, the surface charge has time to accumulate on the electrode and screen the electric potential; at high frequencies, insufficient time occurs for a surface charge to accumulate before reversal of polarity, so the net force exerted by the electric field is negligible [35].

Both ET flow and ACEO are commonly observed as vortical fluid flows depending on the electrode geometry [40,41]. Such vortical flow was observed during both previous proof-of-concept experiments and the well-based experiments of this study. It was expected that convective motion of the fluid due to these EHD effects would carry suspended particles from the bulk fluid volume (where the DEP force is very weak) nearer to electric field non-uniformities around the nanofibers (where the DEP force is sufficient for trapping), thereby enabling the trapping of those particles and improving overall electrokinetic trapping performance. There are several resources available that provide a more in-depth discussion of ET flow and ACEO [7,35,39]. Qualitative

visualizations of ET and ACEO flow directions in a commonly seen non-uniform electric field system utilizing interdigitated planar electrodes are shown in Figure 6.
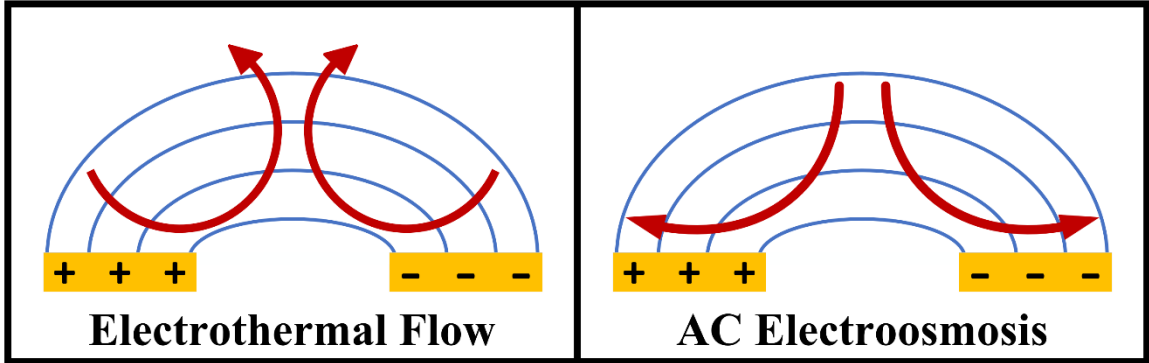
Figure 6. Qualitative visualizations of fluid flow patterns for ET flow and ACEO around interdigitated planar electrodes. Red arrows indicate fluid flow, and blue curves represent electric field lines.

Trapping criteria

A common assumption in microfluidic particle trapping is that a particle subjected to an external force will instantaneously reach its terminal velocity [42,43]. This assumption is valid because the characteristic inertial timescale of micro- and nanoparticles is typically on the order of 10^{-6} s or smaller [35]. The terminal velocity of the particle is typically determined as the velocity at which the applied external force is equal in magnitude to the Stokes drag force given by [6]

$$F_d = 6\pi\mu a v \tag{5}$$

where v is particle velocity.

In absence of other external forces and assuming neutral buoyancy, an applied force must overcome only Brownian diffusion to effectively trap a particle. The fulfillment of this criterion can be verified by comparison of the terminal velocity due to the applied force and the particle velocity due to Brownian motion. Assuming the diffusion velocity is equal to the root mean square Brownian displacement over the

duration of one second, the requisite "trapping velocity" to overcome diffusion must

exceed [6]

$$v_{BM} = \sqrt{\frac{k_B T}{3\pi\mu a}} \tag{6}$$

where k_B is Boltzmann's constant and T is absolute temperature. This criterion

determines the minimum DEP force that would be required to trap a particle in absence of

other EHD effects.

Because the DEP force is a function of the spatial field gradient, it decays

exponentially as distance from the point of sharp electrode geometry which generates the

high field gradients (e.g. a single nanofiber or the corner of a planar electrode) increases.

Therefore, for a given particle, medium, and applied field, one can determine a

theoretical "effective trapping range" around a sharp electrode feature within which the

DEP force is sufficiently great to trap a particle and outside of which a particle will not

become trapped. This implies the trapping efficiency of a DEP system could be improved

by increasing the number of particles which come within the effective trapping range of

the electrode. If the trapping range cannot be increased (e.g. through increasing field

strength) this could also be accomplished by restricting the flow path nearer to the

proximity of the electrode or disturbing the flow field such that more fluid streamlines

pass near the electrode. However, implementing these strategies might incidentally result

in flowrate reduction, which itself would decrease overall trapping throughput.

The anticipated advantages of using CNF mat electrodes in a DEP trapping

system were multifold. First, the sharp geometric features of the nanofibers would

increase field gradients and, by extension, the effective particle trapping range relative to

microfabricated electrodes. Second, the porosity of the mats would enable flowthrough

trapping configurations in which the particle suspension is passed directly through the

mat. This would necessarily bring more particles within a few microns of the electrodes,

depending on pore size, increasing the likelihood of each particle becoming trapped.

Finally, the anticipated vortical flow patterns from EHD effects would agitate the flow

such that particles would take a tortuous path around and/or through the CNF mat, thus

even further increasing the likelihood of trapping.

CHAPTER III

MATERIALS AND METHODS

Microfluidic well device

Electrospun carbon nanofibers

Two CNF mats created using the previously discussed fabrication process were

used for the study described herein. The mats were ~80 μm in thickness with electrical

conductivity measured via a four-point probe at 2.55 S/cm, and the fibers' diameters were

measured at 267 ± 94 nm from SEM images as seen in Figure 7 [13]. Round disks of the

CNF mats 4 mm in diameter were punched from the bulk mat for the fabrication of a

well-based testing device. The punching process did not require significant force, as the

CNF mats were relatively fragile after carbonization. The CNF mat shown in Figure 7

had fiber diameters measured between 300 – 800 nm; the CNF mats used in this study

were created using the same electrospinning parameters as the one shown in Figure 7.
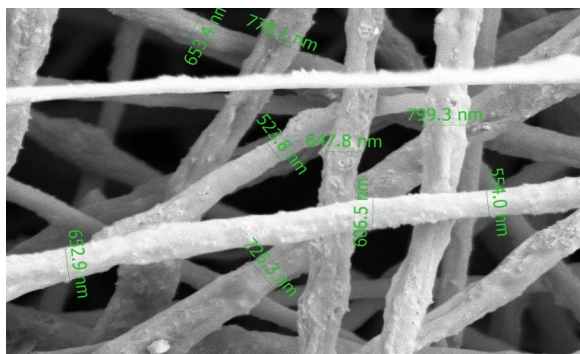
Figure 7. SEM image of conductive nanofiber mat from previous experiments with scale
bars on individual fibers to show size distribution.

Multiple design iterations of a well-based testing device were created before arriving at a final design. The overall architecture of the well-based device approach included the following: a bottom conductive surface to which an electrical connection could be made and upon which round disks of the CNF mat could be placed to form the base of the wells; one or more layers of double-sided adhesive (DSA) to provide adhesion between layers and to seal the wells from leakage; and an upper conductive layer with an array of uniformly sized holes to serve as an opposing electrode and to form the lateral walls of the cylindrical wells. Figure 8 shows three of the major design iterations that preceded the final design.
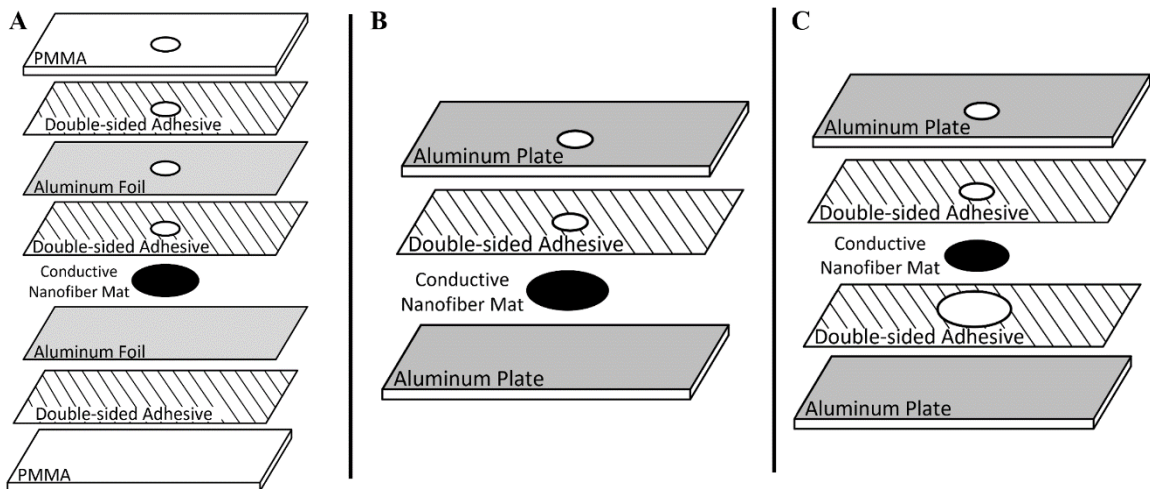
Figure 8. Exploded view schematics of sequential design iterations of the electrokinetic well device. (A): The first iteration which used aluminum foil for the upper and lower electrode surfaces and PMMA sheets to provide rigidity. Holes were manually drilled through all top layers after assembly. (B): A simplified design in which aluminum plates were introduced to provide both conductivity and rigidity, with a single layer of DSA for adhesion and manually drilled holes for the wells. (C): A design which reintroduced a second DSA layer and utilized a cutter plotter to pattern holes in the DSA layers. Holes in the aluminum sheet were again drilled manually.

The design shown in Figure 8A suffered from multiple flaws, chief among these being the excessive complexity of the assembly due to the necessity of three DSA layers

and two sheets of aluminum foil (Al). Furthermore, the process of drilling the holes

through the PMMA, DSA, and Al foil layers invariably caused delamination and

infiltration of PMMA swarf between layers. This resulted in excessive fluid leakage

between wells and compromised the repeatability of the experiments.

The design shown in Figure 8B was a significant step forward in simplicity of

assembly, with only a single sheet of DSA being used to provide adhesion between the

layers. However, the nonuniformity of surface profile caused by the CNF mat disks

sitting atop the bottom Al sheet prevented the DSA from adequately sealing the wells,

resulting in continued leakage. This design also experienced electrical shorting between

the CNF mat and aluminum sheet, which would have compromised experiments.

Figure 8C shows the penultimate design architecture. A second sheet of DSA,

with holes patterned using a cutter plotter, was implemented to prevent leakage between

layers and ensure electrical separation of the opposing electrodes. Determining an

appropriate thickness of this lower DSA layer required multiple design iterations. It was

determined the optimal DSA thickness for this layer was slightly less than the thickness

of the CNF mats so the mats would be compressed into the lower Al sheet by the upper

layers of the assembly, ensuring a uniform electrical connection. Iterations using thicker

DSA in this layer (~82 µm) resulted in inconsistent electrical connections between the

mats and the bottom conducting layer due to lack of this mechanical compression. This

design still suffered from well leakage between the bottom Al sheet and DSA layers.

This was likely due to insufficient adhesion of the DSA to the Al sheet preventing a

complete seal. The other major flaw of this design was the limited precision and

repeatability with which holes could be drilled through the top aluminum sheet using a

drill press. The drilled holes were not precisely patterned, and they were inconsistent in

the formation of burrs around the sharp edges. This caused electrical shorting and limited

repeatability. The final design solved these remaining issues by replacing the bottom Al

sheet with and ITO coated glass slide and the upper Al sheet with a commercially

available perforated Al sheet.

Final design
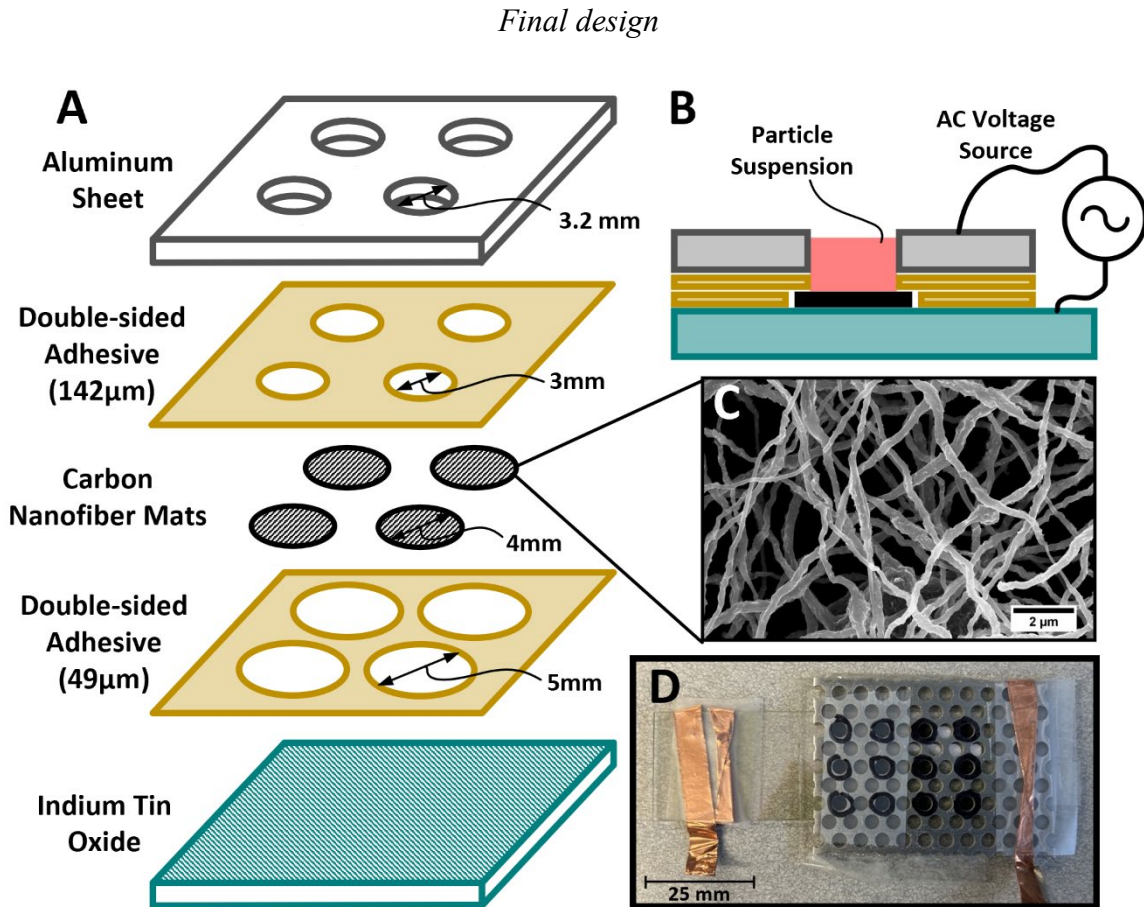
Figure 9. Exploded view (A) and cross-section view (B) of the well-based device schematic used for dielectrophoretic particle trapping, including an SEM image of the CNF mat (C) and an image from the top side of one of the assembled devices (D).

The well-based devices used to characterize the CNF mats' electrokinetic

behavior were fabricated without the use of specialized equipment or cleanroom

procedures. An image of one of the tested devices is shown in Figure 9D, and schematics

of the devices' exploded and cross-sectional views can be seen in Figure 9A and 9B,

respectively. The top layer of the device was a 0.063-inch thickness sheet of 5052

aluminum perforated with an array of 0.125-inch (3.2 mm) diameter holes (McMaster-

Carr item no. 5250N37); all holes patterned into the DSA layers were designed to align

with the aluminum sheet's perforations. This aluminum sheet served as the opposing

electrode to the CNF mats. A glass slide with an indium tin oxide (ITO) coating (8-12 Ω,

SPI Supplies) was the bottom layer of the device.

The 4 mm diameter CNF mat disks were arrayed atop the ITO such that a single

electrical connection to the ITO also connected to every CNF mat disk in parallel. Two

separate layers of DSA were layered between the aluminum sheet and the ITO slide +

CNF mat array. Both DSA layers were patterned with an array of holes using a cutter

plotter (Roland CAMM-1 GS-24). The first lower layer, which adhered to the ITO slide,

had a thickness of 49 µm (Adhesives Research ARcare 92712) and hole diameters of 5

mm. This size allowed the 4 mm CNF mat disks to lie within the holes of this layer. The

second DSA layer, which adhered to the aluminum sheet, was 142 µm thick (Adhesives

Research ARcare 90880) and patterned with holes 3 mm in diameter. This layer ensured

uniform electrode separation between the CNF mats and the aluminum sheet; it also

compressed the CNF mat disks' edges to ensure a uniform electrical connection to the

underlying ITO. Adhesive copper tape was used to aid in connecting the device's

electrodes to electrical equipment.

In practice, the fabrication process was performed starting with the aluminum

sheet, then aligning and applying the remaining layers on the underside of the aluminum

and ending with the ITO slide. The device's construction allowed liquid samples to be

added and removed from the wells without altering the electrode arrangement or

electrical connections. After fabrication, connections were tested to ensure no electrical

short had occurred between the opposing electrodes. Each device was fabricated with

between 12 – 21 wells, which could be used individually for testing various electric field

parameters across repeatable trials. Qualitative visualizations of expected electric field

lines in the test device at the scale of the entire well and at the scale of individual

nanofibers are shown in Figure 10.
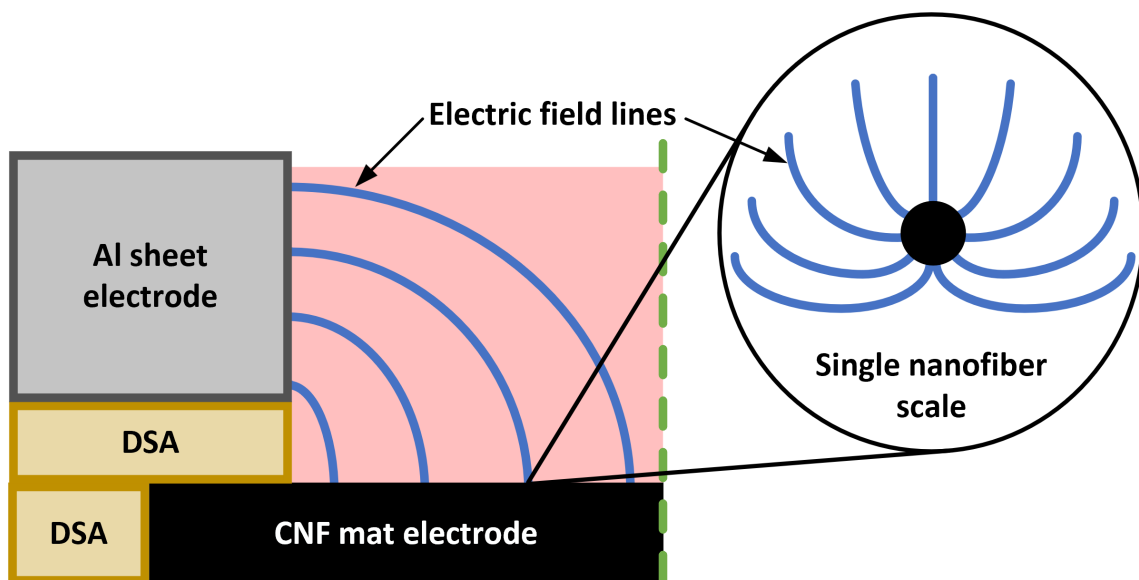
Figure 10. Qualitative visualization of electric field lines in a microfluidic well on the scale of the entire well and a detail view of electric field lines around a single nanofiber. The well is axisymmetric about the green dashed line.

Sample preparation

The tested sample was a suspension of 1.0 µm red fluorescent polystyrene

microspheres (Fluoro-Max, initially 1% solids). The sample was prepared by adding two

drops (approximately 20 µL) of the packaged particle suspension to 5 mL of DI water

(filtered from Milli-Q ultrapure water system) with 0.1% Tween 20 (Thermo Scientific).

Tween 20 is a chemical surfactant added to reduce the surface tension of the suspension

and thereby prevent particle agglomeration. The final particle suspension had a measured

electrical conductivity of 3.08 mS/m (Denver Instrument Model 220 meter). It was noted

that this conductivity was higher than expected for deionized water at this concentration of Tween; however, because the measurement was performed using a well-calibrated conductivity meter, there was confidence in the reported value. Furthermore, subsequent theoretical electrokinetic calculations using this value supported experimental findings. The bulk conductivity of polystyrene microspheres was negligible compared to the effect of the surface conductance, which was taken as $K_s = 2.34$ nS for red carboxylate modified polystyrene microspheres in a suspension with conductivity between $2 - 10$ mS/m as found by Vahey and Voldman [44]. By Eq. 2, this resulted in a calculated total particle conductivity of 9.36 mS/m. The assumed relative permittivity of the medium and particles were $\varepsilon_{r,m} = 78.5$ and $\varepsilon_{r,p} = 2.6$, respectively [45].

Experimental methods

Electrical components

A Keithley 3390 waveform generator was used to supply an AC voltage between the electrodes. The signal from the waveform generator was passed through a Trek 2100HF amplifier. The signal was passed through capacitors both before (3.3 nF) and after (10 nF) the amplifier to act as high-pass filters and remove DC leakage from the electrical signal. An Agilent 34405A digital multimeter was used to measure the signal amplitude and frequency as delivered to the electrodes after being passed through the amplifier and capacitors. An image of the setup with electrical components and microfluidic well device configured as during experiments is shown in Figure 11.
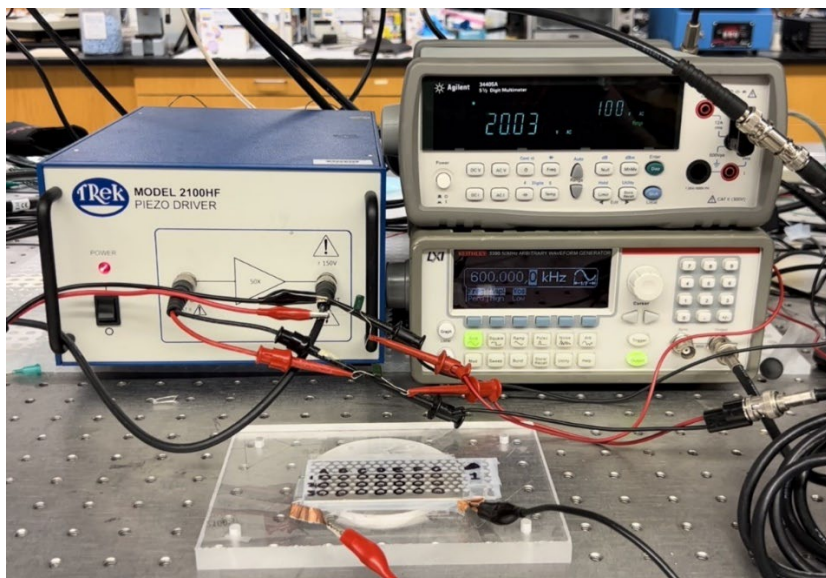
Figure 11. Experimental setup with electrokinetic well devices and electrical components (waveform generator, amplifier, multimeter, and capacitors) configured as during experiments.

Procedure development

Multiple steps in the testing methodology were iteratively improved in parallel with the development of the well device. The first such procedural step was in how the particle suspension was added to the wells for testing. During proof-of-concept experiments described previously, the strips of CNF mats were pre-soaked with DI water before being dipped into the particle suspensions. This step prevented absorption of the particle suspension into the nanofibers, which would have inflated the number of particles trapped within the mat by means other than electrokinetic attraction.

For this study, the microfluidic wells were pre-filled with a consistent volume of DI water + Tween before the addition of the particle suspension. However, it was noted during initial testing that air pockets trapped within and around the CNF mat disk during the assembly process were still present and being slowly displaced by the fluid medium, which caused gradual outward radial flow within the well over the duration of the experiments (~minutes). This also caused particles to become lodged in the mat

unintentionally. Therefore, the additional step of subjecting the well filled with DI water + Tween to a partial vacuum was introduced. Results of subsequent tests indicated this step removed a sufficient portion of the trapped air to make fluid motion negligible.

The selection of test frequencies also required preliminary testing and ultimately resulted in modification of the experimental circuitry setup. In order to study the frequency-dependence of particle trapping performance, it was desirable to conduct experiments at frequencies covering multiple orders of magnitude. Because positive DEP (particle attraction) was known from theory to be greatest at low AC field frequencies (~kHz), the low end of the test frequency range would ideally have been on the order of 10 kHz. However, preliminary particle trapping experiments using field frequencies below 100 kHz consistently resulted in the formation of gas bubbles in the liquid particle suspension. It was hypothesized that this was electrolysis caused by the leakage of a DC signal component through the electrical equipment. This issue needed to be resolved before proceeding with experiments, as the growth of bubbles within the fluid volume would alter the electric field distribution and disturb the fluid volume. As described above, two capacitors were placed in series with the signal to act as passive high-pass signal filters. The appropriate capacitances of these components to use in all particle trapping tests were determined through a trial-and-error process investigating many combinations of available capacitors. With the final configuration, electric fields at 30 kHz with amplitudes as high as 20 V_{rms} could be applied to the wells without the formation of bubbles. The upper bound on testing frequencies was set at 1 MHz due to the limitations of the amplifier used with the signal generation equipment.

Aside from the procedure and equipment modifications described previously, an appropriate time duration for application of the electric fields during the experiments was determined through theoretical analyses and comparison of experimental results. The upper bound on elapsed time was limited by the settling velocity of the suspended particles. A sufficiently short time was required to ensure only a small fraction of suspended particles sedimented into the mat over the duration of each experiment. The terminal settling velocity of the particles was estimated using a Stokes drag assumption as given by Eq. 5, and it was determined that particle settling would be sufficiently low (< 10% of suspended particles reaching the bottom of the well) for experiments with elapsed times less than one hour. This provided flexibility in conducting trials on the order of minutes in length. After conducting preliminary tests at multiple elapsed times up to 10 minutes, a trial length of 5 minutes was selected as the elapsed time for all subsequent experiments.

Determining the camera settings for digital imaging also required iterative refinement. After experiments were concluded, several wells with trapped particles were imaged using a range of ISO and shutter speed settings to determine selections appropriate for all tested wells. The important consideration at this stage was to image all wells using consistent imaging settings under the same illumination scheme so that collected data would enable valid comparisons between trapping performance under different electric field conditions. Therefore, the setting selections required some compromise between the ideal settings for wells with high numbers of particles and those with fewer particles. For example, overexposure could result in measurement noise, whereas underexposure might cause trapped particles to go uncounted during image

analysis. Several images captured using different settings were compared qualitatively, and selections were made accordingly and afterward applied consistently.

Critical values for thresholding and pixel island removal steps in the image analysis routine were determined similarly to the digital image settings. While the pixel intensity cutoff selection was somewhat arbitrary, several values between 0.05 and 0.2 were applied to a selection of well images to evaluate what threshold would accurately represent the data each image contained across the range of results. The small pixel island removal cutoff was selected to remove spurious high-intensity pixels and groups of pixels smaller than individual particle images from the images without removing imaged particles themselves. The threshold for this step was also chosen qualitatively, but knowledge of geometrical optics informed an appropriate selection. It is known that the diffraction of light will cause an optically imaged microparticle to appear larger than its true size [46], so small pixel islands could be safely removed without eliminating the images of trapped particles. It must be noted that the digital imaging and image analysis criteria were not "optimized" per se, as it was necessary to compromise between the combination of settings that would have been ideal for individual well images. Critically, the intensity threshold and minimum pixel island size selections were applied consistently during image analysis to permit comparisons between the results of all experimental trials. Both of these practices served to increase the signal-to-noise ratio of the data contained within the captured images.

Testing procedure

Tests were performed with liquid in only one well at a time so that the sequence of applied voltages and AC frequencies could be randomized for repeated experiments.

Liquids were added to the wells using a micropipette. Initially, 10 µL of DI water with 0.1% Tween 20 was added to pre-soak the CNF mat. With the DI water added, the device was placed under vacuum in a glass desiccator for 5 minutes to evacuate air pockets within and around the CNF mat. Following this, 4 µL of the microsphere suspension was pipetted into the well without removing the original fluid volume. An AC potential was applied between the ITO and aluminum sheet for 5 minutes, at which time the waveform generator output was disabled. Then the fluid, as well as the remaining suspended microspheres, were removed from the well by gently inserting a cotton swab into the well for approximately 5 seconds. It was assumed that trapped particles would remain adhered to the mat during this step based on observations from previous experiments.

AC frequencies of 30 kHz, 100 kHz, 300 kHz, 600 kHz, and 1 MHz were applied with a potential of 20 V_{rms} across the electrodes. Control tests involved the same procedure, excluding the application of an electric field. Tests were repeated with each combination of electric field parameters on six (6) wells. The sequential order of conducted experiments was randomized to avoid any bias related to the well location or variation between the manual fabrication of different devices.

Data collection and analysis

The wells were allowed to dry completely before being digitally imaged. A Nikon Eclipse Ti inverted fluorescent microscope with a 3X total magnification was used with an XCite 120 for illumination. The white light illumination was passed through a DsRed filter cube to view the fluorescent microspheres trapped by the CNF mat. The wells were photographed using a Canon Eos Rebel T7i (6000 × 4000, 3.72 µm/pixel) digital camera using ISO 6400 and 1/15 second shutter speed.

A MATLAB image analysis script (see Appendix for code) was used to process the data from the digital images. Each image was converted to grayscale, and a circle was fitted to the perimeter of the well based on five user-selected points on the well's edge. The image was then cropped to include only pixels inside the circle. From there, each pixel was assigned the binary value 0 or 1 if its lightness was below or above, respectively, a threshold of 0.15. Pixel islands smaller than 20 pixels in size were removed from the images, as such features would be smaller than the size of a single particle image and thus represent only measurement noise. Then each remaining white pixel was counted and assigned a value between 0 – 1 based on its normalized radial distance from the center of the well. The pixel count of each image was used as the metric for comparison of particle trapping between different electric field frequencies. To avoid noise in the data associated with particles stuck to the sharp edge of the aluminum sheet, white pixels from the outer 20% of the circle by area (0.8944 – 1 by normalized radius) were excluded from the final pixel counts. Chauvenet's criterion was then applied to remove statistical outliers from each group [46]. Figure 12 shows sample images from intermediate steps of the digital image processing procedure.
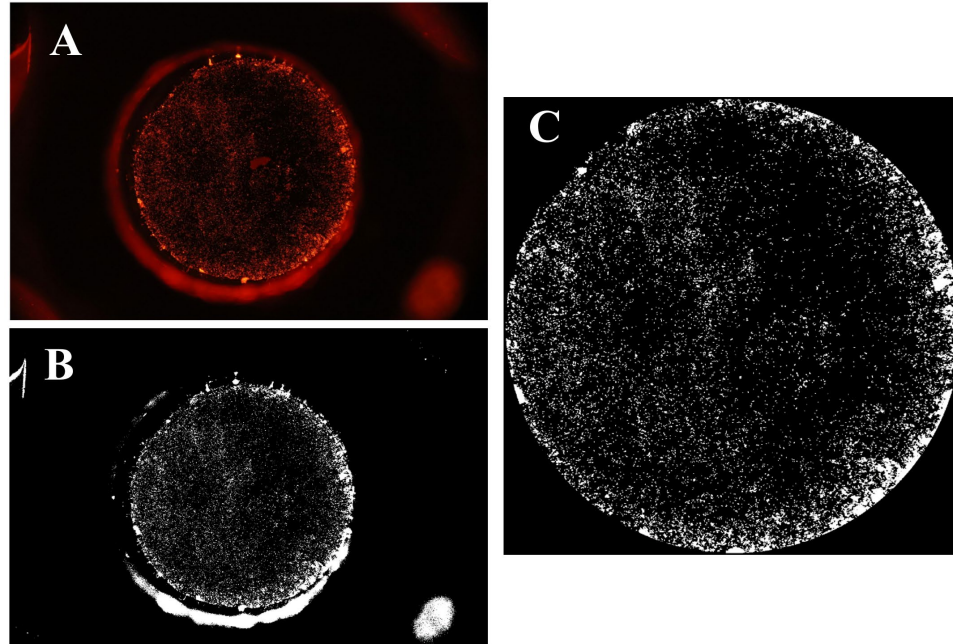
Figure 12. Sample MATLAB image analysis steps as described in the primary manuscript. (A): An unaltered digital image of a microfluidic well tested with a 600 kHz electric field at an applied voltage of 20 V_{rms}. (B): The same image binarized using the uniformly applied threshold level of 0.15. (C): The final image cropped to include only the CNF mat and with pixel islands smaller than 20 pixels in size removed.

CHAPTER IV

RESULTS AND DISCUSSION

Expected behavior

The electric field frequencies for these experiments were chosen to span a range of

$Re[CM]$ values. At the low frequencies (30 kHz, 100 kHz), the magnitude of the DEP

force was near its greatest intensity. Conversely, the higher frequencies (600 kHz, 1

MHz) were selected to exhibit lower DEP strength. Figure 13 shows theoretical Re[CM]

(Eq. 1) plotted against AC frequency using the referenced and measured dielectric

properties of the media and materials for this study.
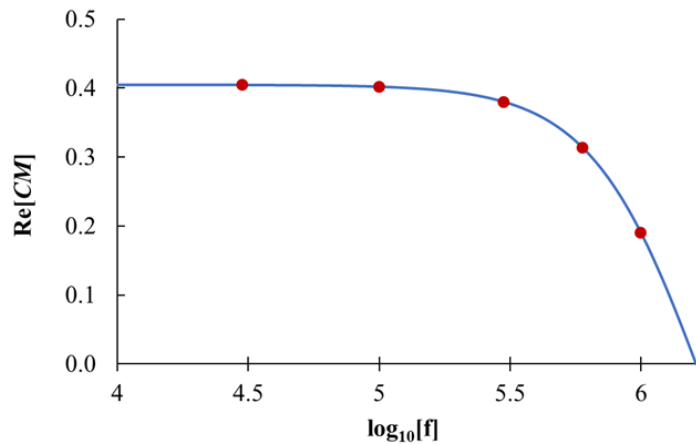
Figure 13. Re[CM] vs. log(f) for fluorescent microspheres of conductivity 9.36 mS/m and relative permittivity 2.6 within medium with conductivity 3.08 mS/m and relative permittivity 78.5. Red markers indicate electric field frequencies used in experiments.

The intensity of other EHD phenomena (ET flow, ACEO) was also known to decay

with increasing field frequency. Based on the expectation that all EHD phenomena

contributed positively to particle trapping by circulating particles within the effective

35

trapping range of the nanofibers, it was assumed that the number of trapped particles would decrease as AC frequency increased. As all test frequencies were within the range in which $Re[CM] > 0$, it was expected that all test groups would effectively trap particles to some degree, whereas the control group with no applied electric field would show comparatively low numbers of particles.

Due to the well-based electrode configuration of the device, it was assumed that electric field strength (and thus the effective trapping range around individual nanofibers) would be greatest near the perimeter of the wells, with both field strength and trapping performance decreasing toward the centers of the wells. It was therefore assumed that more trapped particles would be observed near the well perimeters than in the centers for all trapping frequencies.

<div align="center">Observations</div>

Observation of activity within the microfluidic wells during experimentation was made difficult by the optical distortion from the fluid meniscus. This distortion made quantitative techniques for measuring particle motion such as particle image velocimetry impractical to implement. Qualitative observations did provide insight regarding the presence of EHD motion during the particle trapping experiments. It was clear despite optical distortions that vortical fluid flow characteristic of electrothermal hydrodynamic motion was present [40]. However, it was unclear whether this motion contributed positively or negatively to particle trapping from these observations alone.

The wells were also observed during the moment at which the applied electric field was removed. As expected, particle motion rapidly decayed, and particles trapped by the CNF mat did not appear to move away from the nanofibers. This was consistent with

expectations, as particles were also observed to have a tendency to remain trapped within the CNF mat after removal of the electric field during proof-of-concept experiments as described in [13]. It was hypothesized that this sticking was due to electrostatic attraction resultant from surface charges, van der Waals forces, and/or mechanical impaction of particles within CNF mat pores, but these hypotheses were not investigated further. Ultimately, it was decided the repeated procedural treatment of each microfluidic well permitted the statistical comparison of particle counts for assessment of electrokinetic trapping performance.

Results

Images of one well from each experimental group are shown in Figure 14A-F. The images chosen to represent each group were those in which the white pixel count (excluding the outer 20% of the well by area) was nearest to the mean for their respective group. Figure 14G shows a graph of average counted pixels among wells in each experimental group. The greatest numbers of trapped particles appeared near the perimeters of the wells where electric field strength was greatest, as predicted. Furthermore, with data from the entirety of the well images included in the analyses, all test groups showed trapped particles in significantly greater quantities than the control group in which no electric field was applied. The particles trapped in the control group CNF mats were likely due to diffusion, sedimentation, and/or electrostatic attraction. These observations were all consistent with expectations.
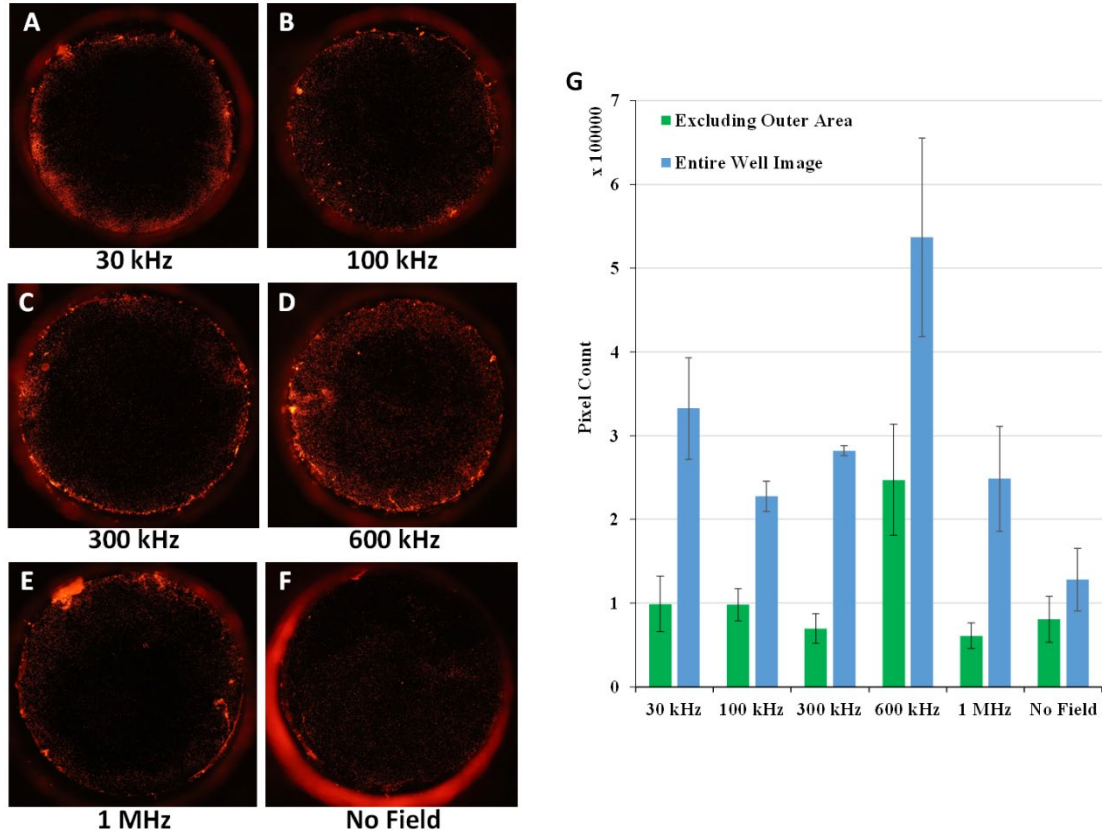
Figure 14. (A-F): Representative images of microfluidic wells showing fluorescent microspheres trapped using a range of electric field frequencies with an applied potential of 20 V_{rms}. Images were chosen such that the trapped particle pixel count was nearest to the respective group average. (G): Average counted pixels for well images in each test frequency group after outliers removed. Data are shown for counts of the entire well image as well as counts excluding the outer 20% of the well by area. Error bars show standard error ($\sigma/\sqrt{n}$).

By contrast, it can be seen from both Figure 14D and 14G that the most significant particle trapping occurred at 600kHz, which was notably inconsistent with expectations. It was noted that for the data including only pixels within the inner 80% of the wells by area, the 600 kHz group was the only group in which a significantly greater number of particles were trapped than in the control group. Therefore, it was apparent that across the interior region of the CNF mat where electric field strength was weakest, DEP trapping was insignificant at all other field frequencies. Stated another way, it was indicated by the results that across the interior surface of the mat, the greatest trapping

performance occurred at 600 kHz despite the relative weakness of DEP compared to lower test frequencies. Therefore, it was evident that some other effect was reducing the trapping performance of the CNF mats at the other test frequencies. This was a notable result that warranted further investigation of the relevant EHD phenomena.

<div align="center">Electrohydrodynamic effects</div>

A qualitative analysis of the directions of the various relevant EHD phenomena was conducted to investigate whether trapping might be hindered by their influence. For the experimental setup described herein, the induced motion of a particle by each phenomenon at the scale of individual carbon nanofibers (in absence of other effects) is shown in Figure 15.
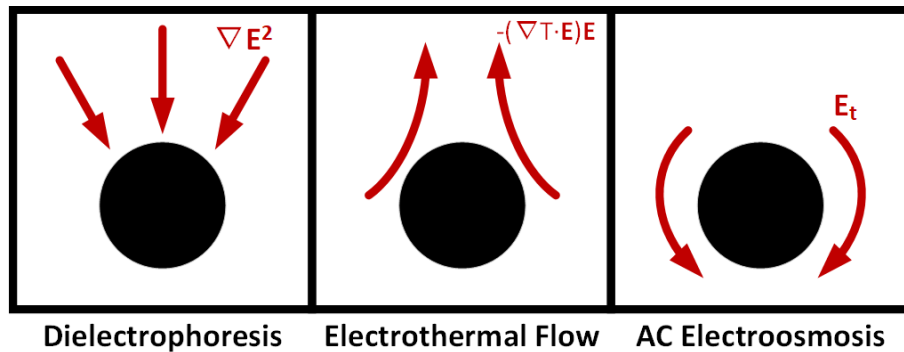
Figure 15. Qualitative visualization of induced particle motion at the scale of a single CNF. Black circles represent the cross-section of a fiber oriented axially into the page, and red arrows indicate the expected particle motion in absence of other phenomena.

It was noted that the effect of ET flow and ACEO on trapping performance might not be simply positive or negative as with DEP. Therefore, the frequency dependence of the ET flow and ACEO magnitudes were compared to that of DEP over the frequency range of the experiments. For this analysis, the frequency-dependent components in the analytical functions for each phenomenon were normalized by their respective maximum values to determine a relative magnitude of each effect as a function of field frequency. Note that this analysis does not provide insight into the comparative magnitudes of each

phenomenon (i.e. a given relative magnitude of one phenomenon should not be thought of as equal in strength to the same relative magnitude of another phenomenon). It should be further emphasized that while all relevant phenomena decay in strength with increased distance from the nanofibers, these distance dependencies are not equivalent. For DEP, the relative magnitude is simply $Re[CM]$ normalized by its own maximum value, which occurs theoretically as electric field frequency $f \to 0$. For this analysis, $Re[CM] \approx 0.4$ was the theoretical maximum. Calculating the theoretical relative magnitudes of ET flow and ACEO was a more involved process, as discussed in the following sections.

Electrothermal hydrodynamics

The theoretical expression for the time-averaged volume electrothermal hydrodynamic force is given by [47]

$$\langle f_e \rangle = \frac{1}{2} Re \left(\frac{\sigma_m \varepsilon_m (\alpha - \beta)}{\sigma_m + i\omega\varepsilon_m} (\nabla T \cdot E)E^* - \frac{1}{2}\varepsilon_m\alpha|E|^2\nabla T \right) \tag{7}$$

where E and E^* are the electric field and its complex conjugate, respectively, and ∇T is the spatial gradient of the temperature field. Fluid property-derived constants $\alpha = (\partial\varepsilon_m/\partial T)/\varepsilon_m \approx -0.0046 \ K^{-1}$ and $\beta = (\partial\sigma/\partial T)/\sigma \approx 0.020 \ K^{-1}$ for aqueous solutions were used [47]. Using the simplifying assumption $(\nabla T \cdot E)E^* \approx |E|^2\nabla T$, one can reduce the frequency-dependent relative magnitude of the electrothermal force to

$$\frac{\langle f_e \rangle}{\langle f_{e,max} \rangle} = \frac{1}{\varepsilon_m \left(\frac{1}{2}\alpha - \beta\right)} \left(\frac{\sigma_m^2 \varepsilon_m (\alpha - \beta)}{\sigma_m^2 + (\omega\varepsilon_m)^2} - \frac{1}{2}\varepsilon_m\alpha \right) \tag{8}$$

. It can be seen that this magnitude reaches its maximum for $\omega \to 0$ similarly to $Re[CM]$. For the fluid medium used in this study, electrothermal relaxation (the theoretical point of zero ET flow velocity) occurs at an electric field frequency $f \approx 2.4$ MHz.

AC electroosmosis

For the theoretical analysis of ACEO magnitude, the CNF mat and aluminum sheet electrodes were analogized to interdigitated planar electrodes. For a series of interdigitated planar electrodes in a traveling wave electroosmotic pumping system, the AC electroosmotic slip velocity is given by [7]

$$\langle u_s \rangle = \Lambda \left(\frac{\varepsilon_m k V_0^2}{2\mu} \right) \left(\frac{\Omega}{1+\Omega^2} \right), where\ \Lambda = \frac{C_s}{C_s + C_d}, and\ \Omega = \omega \left(\frac{C_{DL}}{k\sigma_m} \right) \tag{9}$$

where k is the spatial angular frequency and V_0 is the amplitude of the applied AC potential. C_s, C_d, and C_{DL} are the capacitances of the compact layer, the Debye layer, and the entire electric double layer, respectively, which are related by $C_{DL}^{-1} = C_s^{-1} + C_d^{-1}$ [7]. Because the electroosmotic slip velocity function has a maximum at $\Omega = 1$, the expression for the relative magnitude of ACEO simplifies to

$$\frac{\langle u_s \rangle}{\langle u_{s,max} \rangle} = \frac{2\Omega}{1+\Omega^2} \tag{10}$$

. Based on the typical aspect ratio of the fibers in the CNF mat, and extrapolation from results presented in [48], a CNF double layer capacitance of $C_{DL} = 0.05$ F/m^2 was used. The appropriate spatial angular frequency related to electrode spacing for this analysis was ambiguous due to the nonuniform electrode spacing between the surface of the CNF mat and the edge of the perforated hole in the aluminum sheet. Therefore, several potential values in a range $2,000 \frac{rad}{m} \leq k \leq 25,000 \frac{rad}{m}$ representing opposing electrode spacings between 142 μm (the DSA spacer thickness) and 1.5 mm (the microfluidic well radius) were considered. For all values in this range, the peak electroosmotic slip velocity occurred at a field frequency less than 1 kHz, and the ACEO relative magnitude had decayed to < 2% for all frequencies used in this study. Performing tests at

frequencies near that of the peak slip velocity was not feasible due to the onset of

electrolysis at frequencies less than 30 kHz.

Comparisons

The relative magnitude of ACEO was shown to reach its peak at a field frequency

less than 1 kHz, above which it decayed rapidly. For all tested frequencies, ACEO was

reduced by 98% or more relative to its maximum intensity. Therefore, it was concluded

that ACEO likely did not significantly affect the results of the experiments either

positively or negatively. Investigating frequencies at which ACEO might be at a relevant

magnitude was not feasible with the experimental setup used, as applying field

frequencies lower than 30 kHz consistently resulted in rapid electrolysis of the sample.

By contrast, the relaxation of the electrothermal flow occurred primarily within the range

of frequencies used in this study. Plots of the relative magnitudes of DEP and ET flow
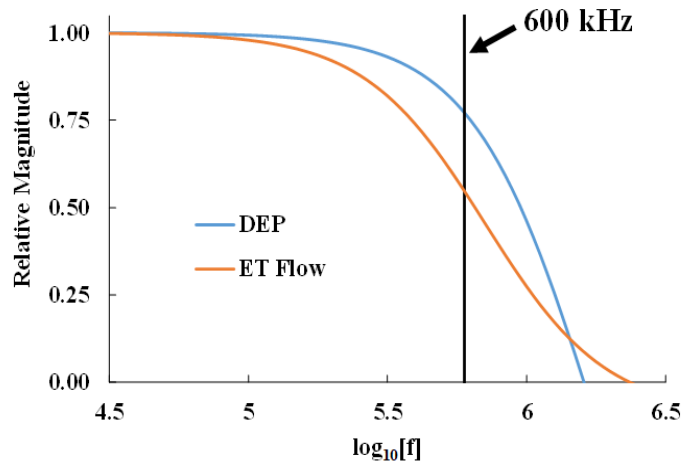
are shown in Figure 16.

Figure 16. Plotted normalized magnitudes of dielectrophoresis and electrothermal flow across the range of electric field frequencies used in this study.

The maximum trapping frequency of 600 kHz is specifically called out in Figure

16. It was noted that at that frequency, the ET flow relative magnitude had begun to

42

decay significantly (~0.55) whereas that of DEP had decayed comparatively less (~0.77). At the lower test frequencies, both DEP and ET flow were near their greatest intensity. At 1 MHz, while ET flow had decayed even further (~0.27), the DEP had also undergone significant reduction in magnitude (~0.46). This analysis indicated 600 kHz may have been the most effective trapping frequency because ET flow had decayed without a likewise reduction in DEP. The distance dependencies of the two phenomena in relation to the CNF mats are not equivalent because they are functions of different gradients (∇T for ET flow and ∇E for DEP, broadly speaking). Therefore, direct comparisons between the strengths of the phenomena would be non-trivial. However, an interaction effect dependent upon the comparative values of their relative strengths may explain the significant increase in particle trapping at 600 kHz.

Net effects

It is understood that positive DEP will contribute exclusively positively to trapping as its force acts only toward the electrodes where both field strength and spatial gradients are greatest by definition. As stated previously, the effect of ACEO is inconclusive, as it would have been negligible at all tested frequencies in this study. As such, further studies would be required to assess the effect of ACEO on electrokinetic particle trapping.

As stated above, the effect of ET flow was previously expected to be positive regardless of magnitude (and thus at all frequencies) because the circulatory motion would carry particles from the bulk fluid to regions within the trapping range of the fibers. However, it is plausible that if the ET flow was too strong, the trapping force of the DEP within portions of the theoretical trapping range would be insufficient to

43

overcome inertial effects and dislodge particles from the ET flow streamlines. In such a case, the experimental trapping range of the fibers would be reduced by the ET flow, negating the positive effect of particle circulation. If the ET flow velocity were reduced, however, the trapping force required to overcome the particles' inertia would likewise be reduced, increasing the effective trapping range. Therefore, the trapping performance might be dependent upon an interaction effect between the comparative strengths of DEP and ET flow which could be optimized to produce the maximum particle trapping rate for a given system. With increasing ET flow velocity, the effective trapping range around the nanofibers would be reduced; at the same time, however, the greater rate of fluid circulation would introduce more particles to the regions of effective trapping. Therefore, the optimal trapping frequency might be found at a point of compromise between these competing frequency-dependent effects. This hypothesis would explain the results of the study. Such a result was unexpected, and as such the electric field parameters had not been selected with the intent to study this effect.

Based on the results of the study and subsequent theoretical analyses, it appears likely that a field frequency of 600 kHz was more advantageous for particle trapping across the bulk area of the mat than the other test frequencies because ET flow was reduced in strength somewhat more than DEP. This is not to say that 600 kHz was the optimal trapping frequency, and the optimization problem would likely also be dependent upon electrode geometry in addition to the fluid medium and particle properties.

Conclusions

Despite the unexpected results, the primary goals of the study were accomplished. First, the microfluidic well-based testing device enabled repeatable experiments to be

performed to assess the electrokinetic particle trapping performance of CNF mat electrodes. The same platform could be adapted for characterization of and comparisons between different CNF electrodes and to assess variability in performance among specimens fabricated using identical procedures. Repeatability and lack of sophistication in conducting such experiments was one of the study's primary goals, and the final device design fulfills both requirements.

Additionally, the results of the study improved understanding of the interaction between EHD phenomena in electrokinetic trapping systems utilizing CNF electrodes. Specifically, the study found that ET flow can contribute negatively to DEP particle trapping performance depending on its magnitude relative to DEP. In practice, this implies optimization of particle trapping for a given system may occur at field frequencies other than those at which the DEP force is maximized depending upon the magnitude and frequency dependence of ET flow. This finding was notably contrary to previous assumptions. While future work will be necessary to fully understand the interactions between DEP, ET flow, and ACEO with respect to their effects on trapping performance, this study could inform the direction of subsequent work on the subject and guide the selection of experimental parameters in future studies.

Future work

The experimental results and theoretical analysis provided evidence that electrothermal hydrodynamics can negatively affect the CNF mats' electrokinetic particle trapping in specific circumstances. Future numerical simulations and experimental work should further investigate the effect of ACEO and ET flow on the electrokinetic particle trapping performance of CNF mats. Better understanding these effects would inform the

design of electrokinetic filtration devices and the selection of electric field parameters for maximum efficiency and throughput.

To further investigate the effect of ACEO experimentally, an electrical setup would need to be developed in which low field frequencies ($\lesssim 10$ kHz) could be tested without inducing electrolysis or otherwise degrading the particle suspension or electrodes. To accomplish this, electrochemical effects would need to be considered during the device design and selection of experimental parameters (e.g. reactions at the metal electrodes, magnitude of applied potential, etc.). Based on the theoretical qualitative visualization of induced flow direction around a conductive nanofiber shown in Figure 15, ACEO would be expected to contribute positively to trapping performance in at least some scenarios. However, the possibility of significant negative effects from high-strength ET flow at low frequencies (where ACEO is maximized) might negate any beneficial effects of ACEO.

The effect of ET flow on particle trapping could be further investigated through numerical simulation. A simulation of unidirectional flow through a microchannel in which flow passes through an array of conductive nanofibers with an applied potential could provide insight into the competing contributions of DEP and ET flow. Based on the results of this study, it would be expected that optimal trapping might occur at frequencies within the positive DEP range for which ET flow is present but weakened. The effect of particle and fluid medium electrical conductivities might also be explored in this way. For the experimental trials of this study, trapping might have been expected to improve at all frequencies with a lower conductivity fluid medium. Robust data sets resulting from such models could inform the selection of optimal electric field parameters

for combinations of particles and fluid media for maximizing throughput of electrokinetic trapping systems.

The methodology described herein might also be used to characterize the trapping performance of different nanofiber mat samples and compare trapping ability between mats. Electrospinning setup parameters can be tuned to achieve different mat geometric characteristics (fiber diameter, pore size, etc.). Additionally, mats can be made electrically conductive by other means than pyrolysis. One example the group has already begun exploring is the deposition of sub-micron thickness metal layers onto an electrospun (not carbonized) PAN nanofiber mat through microfabrication techniques such as sputtering [49] or evaporation [50]. This approach would very likely increase the mats' electrical conductivity, making the electric field strength across the bulk interior of the mat stronger. This may serve to increase DEP strength and thus improve the effective trapping range around individual nanofibers.

Other groups have demonstrated the fabrication of nanofiber arrays with highly tunable geometries (diameter, angle, pore size, etc.) [51,52]. Such arrays might also be made conductive through metal deposition processes for use in electrokinetic particle trapping. The variation of CNF mat parameters through these or other means could be investigated using similar methodologies to those used in this study for optimization of electrokinetic particle trapping throughput.

REFERENCES

[1]   In: Environmental Protection Agency. Indoor Air Quality (IAQ): What is a MERV rating? Web. Accessed 31 March 2024. https://www.epa.gov/indoor-air-quality-iaq/what-merv-rating; 2024.

[2]   Hinds W. Aerosol Technology: Properties, Behavior, and Measurement of Airborne Particles. New York, NY, USA: Wiley; 1999.

[3]   Salafi T, Zeming KK, Zhang Y. Advancements in microfluidics for nanoparticle separation. Lab on a Chip. 2017;17:11-33.

[4]   György B, Szabó TG, Pásztói M, Pál Z, Misják P, Aradi B, *et al.* Membrane vesicles, current state-of-the-art: emerging role of extracellular vesicles. Cellular and Molecular Life Sciences. 2011;68:2667-88.

[5]   Global Biofilter Market Size & Share Analysis Report 2030. Grand View Research. Biotechnology. 2023.

[6]   Nguyen N-TW, Steven T.; Shaegh, Seyed Ali Mousavi. Fundamentals and Applications of Microfluidics. 3 ed.; 2019.

[7]   Electrokinetics and Electrohydrodynamics in Microsystems. SpringerWeinNewYork; 2011.

[8]   Sen M, Ino K, Ramón-Azcón J, Shiku H, Matsue T. Cell pairing using a dielectrophoresis-based device with interdigitated array electrodes. Lab on a Chip. 2013;13:3650-2.

[9]   Cho YK, Kim S, Lee K, Park C, Lee JG, Ko C. Bacteria concentration using a membrane type insulator-based dielectrophoresis in a plastic chip. Electrophoresis. 2009;30:3153-9.

[10]   Colburn T, Matyushov DV. Trapping proteins on nanopores by dielectrophoresis. Journal of Applied Physics. 2023;133,164701.

[11]   Mishra A, Gupta K, Wereley ST. Nature of trapping forces in optically induced electrothermal vortex based tweezers. Physical Review Fluids. 2021;6,023701.

[12]   Pesch GR, Du F. A review of dielectrophoretic separation and classification of non-biological particles. Electrophoresis. 2021;42:134-52.

[13]   Mondal TK, West JH, Williams SJ. An electrospun nanofiber mat as an electrode for AC-dielectrophoretic trapping of nanoparticles. Nanoscale. 2023;15:18241-9.

[14]   Lee KW, Liu BYH. On the minimum efficiency and the most penetrating particle-size for fibrous filters. Journal of the Air Pollution Control Association. 1980;30:377-81.

[15]   Tronville P, Gentile V, Marval J. Guidelines for measuring and reporting particle removal efficiency in fibrous media. Nature communications. 2023;14:5323.

[16]   Patel S, Showers D, Vedantam P, Tzeng TR, Qian SZ, Xuan XC. Microfluidic separation of live and dead yeast cells using reservoir-based dielectrophoresis. Biomicrofluidics. 2012;6,034102.

[17]   Giesler J, Weirauch L, Thöming J, Baune M, Pesch GR. Separating microparticles by material and size using dielectrophoretic chromatography with frequency modulation. Scientific Reports. 2021;11,16861.

[18]   Abd Rahman N, Ibrahim F, Yafouz B. Dielectrophoresis for Biomedical Sciences Applications: A Review. Sensors. 2017;17,449.

[19]   Pethig R. Review Article—Dielectrophoresis: Status of the theory, technology, and applications. Biomicrofluidics. 2010;4.

[20]   Li M, Anand RK. Cellular dielectrophoresis coupled with single-cell analysis. Analytical and Bioanalytical Chemistry. 2018;410:2499-515.

[21]   Wood NR, Wolsiefer AI, Cohn RW, Williams SJ. Dielectrophoretic trapping of nanoparticles with an electrokinetic nanoprobe. Electrophoresis. 2013;34:1922-30.

[22]   Barik A, Chen XS, Oh SH. Ultralow-Power Electronic Trapping of Nanoparticles with Sub-10 nm Gold Nanogap Electrodes. Nano Letters. 2016;16:6317-24.

[23]   Sabuncu AC, Liu JA, Beebe SJ, Beskok A. Dielectrophoretic separation of mouse melanoma clones. Biomicrofluidics. 2010;4,021101.

[24]   Farasat M, Chavoshi SM, Bakhshi A, Valipour A, Badieirostami M. A dielectrophoresis-based microfluidic chip for trapping circulating tumor cells using a porous membrane. Journal of Micromechanics and Microengineering. 2022;32,015008.

[25]   Lee HJ, Yasukawa T, Suzuki M, Taki Y, Tanaka A, Kameyama M, *et al.* Rapid fabrication of nanoparticles array on polycarbonate membrane based on positive dielectrophoresis. Sensors and Actuators B-Chemical. 2008;131:424-31.

[26]   Sandison ME, Cooper JM. Nanofabrication of electrode arrays by electron-beam and nanoimprint lithographies. Lab on a Chip. 2006;6:1020-5.

[27]   Madiyar FR, Syed LU, Culbertson CT, Li J. Manipulation of bacteriophages with dielectrophoresis on carbon nanofiber nanoelectrode arrays. Electrophoresis. 2013;34:1123-30.

[28]   Pesch GR, Lorenz M, Sachdev S, Salameh S, Du F, Baune M, *et al.* Bridging the scales in high-throughput dielectrophoretic (bio-) particle separation in porous media. Scientific Reports. 2018;8,10480.

[29]   Lorenz M, Malangré D, Du F, Baune M, Thöming J, Pesch GR. High-throughput dielectrophoretic filtration of sub-micron and micro particles in macroscopic porous materials. Analytical and Bioanalytical Chemistry. 2020;412:3903-14.

[30]   He JH, Liu Y, Xu L. Apparatus for preparing electrospun nanofibres: a comparative review. Materials Science and Technology. 2010;26:1275-87.

[31]   Subbiah T, Bhat GS, Tock RW, Pararneswaran S, Ramkumar SS. Electrospinning of nanofibers. Journal of Applied Polymer Science. 2005;96:557-69.

[32]   Xue JJ, Wu T, Dai YQ, Xia YN. Electrospinning and Electrospun Nanofibers: Methods, Materials, and Applications. Chemical Reviews. 2019;119:5298-415.

[33]   Miao Y-EL, T. Electrospun Nanofiber Electrodes: A Promising Platform for Supercapacitor Applications. In: Electrospinning: Nanofabrication and Applications. William Andrews Publishing; 2019. p. 641-69.

[34]   Pohl HA. The Motion and Precipitation of Suspensoids in Divergent Electric Fields. Journal of Applied Physics. 1951;22:869 - 71.

[35]   Castellanos A, Ramos A, González A, Green NG, Morgan H. Electrohydrodynamics and dielectrophoresis in microsystems:: scaling laws. Journal of Physics D-Applied Physics. 2003;36:2584-97,Pii s0022-3727(03)63619-3.

[36]   Wu JZ. Understanding the Electric Double-Layer Structure, Capacitance, and Charging Dynamics. Chemical Reviews. 2022;122:10821-59.

[37]   Salari A, Navi M, Lijnse T, Dalton C. AC Electrothermal Effect in Microfluidics: A Review. Micromachines. 2019;10,762.

[38]   García-Sánchez P, Ramos, A. . AC Electroosmosis: Basics and Lab-on-a-Chip Applications. In: Encyclopedia of Nanotechnology. 2012.

[39]   Ramos A, Morgan H, Green NG, Castellanos A. AC electric-field-induced fluid flow in microelectrodes. Journal of Colloid and Interface Science. 1999;217:420-2.

[40]   Cao J, Cheng P, Hong FJ. A numerical study of an electrothermal vortex enhanced micromixer. Microfluidics and Nanofluidics. 2008;5:13-21.

[41]   Tiflidis C, Westerbeek EY, Jorissen KFA, Olthuis W, Eijkel JCT, De Malsche W. Inducing AC-electroosmotic flow using electric field manipulation with insulators. Lab on a Chip. 2021;21:3105-11.

[42]   Morgan H, Green NG. AC electrokinetics: colloids and nanoparticles. Research Studies Press; 2003.

[43]   Morgan H, Hughes MP, Green NG. Separation of submicron bioparticles by dielectrophoresis. Biophysical Journal. 1999;77:516–25.

[44]   Vahey MD, Voldman J. High-Throughput Cell and Particle Characterization Using Isodielectric Separation. Analytical Chemistry. 2009;81:2446-55.

[45]   White CM, Holland LA, Famouri P. Application of capillary electrophoresis to predict crossover frequency of polystyrene particles in dielectrophoresis. Electrophoresis. 2010;31:2664-71.

[46]   Tavoularis S. Measurement in Fluid Mechanics. Cambridge University Press; 2005.

[47] González A, Ramos A, Morgan H, Green NG, Castellanos A. Electrothermal flows generated by alternating and rotating electric fields in microsystems. Journal of Fluid Mechanics. 2006;564:415-33.

[48] Molahalli V, Chaithrashree K, Singh MK, Agrawal M, Krishnan SG, Hegde G. Past decade of supercapacitor research-Lessons learned for future innovations. Journal of Energy Storage. 2023;70,108062.

[49] Depla DM, S.; Greene, J.E. Sputter Deposition Processes. In: Handbook of Deposition Technologies for Films and Coatings. 2010. p. 253-96.

[50] Jaeger RC. Film Deposition. In: Introduction to Microelectronic Fabrication. Prentice Hall. p. 129-34.

[51] Nain A. US Patent No. 9029149. In: USPTO, editor. USA: 2015.

[52] Nain A, Behkam B. US Patent No. 9753023. In: USPTO, editor. USA: 2017.

APPENDIX – MATLAB SCRIPT

The following MATLAB code was used for the digital image analysis described herein:

```
%% 1. INITIALIZE, DEFINE VARIABLES
clear; %clear variables
Ithresh = 0.15; % image threshold level for binary, 0-1
removearea = 20; % remove binary pixel islands smaller than
this size
clickpoints = 5; % number of times to click to define
circle fit
rbuffer = 0.00; % reduce cropped circle RADIUS by this, 0.1
= 10%

%% 2. ACQUIRE IMAGE, CONVERT GRAYSCALE
ifile = uigetfile('*.jpg'); % seek file
RGB = imread(ifile); % read file
I = rgb2gray(RGB); % convert to grayscale
BW = imbinarize(I,Ithresh);  % apply threshold

%% 3. IMAGE MODIFICATION
BW2 = bwareaopen(BW, removearea);  % performs small image
removal

% Routine to manually crop circle
figure(1)                    % show figure
%imshow(imcomplement(BW2))    % invert the black/white
image
imshow(I);    % invert the black/white image
[x,y]=ginput(clickpoints);            % click input -
perimeter
a=[x y ones(size(x))]\[-(x.^2+y.^2)];
xc = floor(-.5*a(1));   % center, x-coordinate
yc = floor(-.5*a(2));   % center, y-coordinate
R  =  ceil(sqrt((a(1)^2+a(2)^2)/4-a(3)));   %radius of
circle
Ractual = R*(1-rbuffer);    % new reduced radius of image


% Routine to crop the image to a square with centered
interior circle
```

```matlab
BW3 = double(BW2);
imageSize = size(BW3);
[xx,yy] = ndgrid((1:imageSize(1))-yc,(1:imageSize(2))-xc);
mask = double( ((xx).^2 + (yy).^2)<((Ractual)^2) );
croppedImage = double(zeros(size(BW3)));
croppedImage = BW3.*mask;
croppedImage2 = croppedImage(floor(yc-
R):ceil(yc+R),floor(xc-R):ceil(xc+R));
BW4 = imbinarize(croppedImage2);

%% 4. ANALYSIS
rr = (xx.^2+yy.^2).^0.5 ./ Ractual; % calculate radius as
percentage
rr2 = rr.*mask; % apply mask outside R
rr3 = rr2.*BW3; % multiplied by 0 or 1 from BW3, remaining
values are at white pixels

rrlist = sort(nonzeros(rr3)); % every entry is a white
pixel. Radius location %

writematrix(rrlist,'3G3.csv')

%% 5. PLOTS
figure(2)
imshow(I);

figure(3)
subplot(1,3,1)
imshow(BW);
title('Original')
subplot(1,3,2)
imshow(BW2);
title('Small Removal')
subplot(1,3,3)
imshow(BW4);
title('Cropped')
```

APPENDIX – PERMISSIONS

ROYAL SOCIETY OF CHEMISTRY

Permission Request Form for RSC Material

To request permission to use material from material published by The Royal Society of Chemistry (RSC), please complete and return this form.

From: Name: Jacob Hunter West   E-mail: jhwest02@louisville.edu

Address: 332 W Forestdale Rd

Ashland, KY 41102

I am preparing the following work for publication:

Article/Chapter Title   Electrokinetic particle trapping performance of conductive r

Journal/Book Title   N/A (MS Thesis)

Editor/Author(s)   Jacob Hunter West
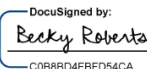
Publisher   N/A (MS Thesis)

I would very much appreciate your permission to use the following material:

Journal/Book Title   Nanoscale

Article/Chapter Title   An electrospun nanofiber mat as an electrode for AC-dielec

RSC Editor/Author(s)   TK Mondal, JH West, SJ Williams

DOI   10.1039/D3NR04496C

Year of Publication   2023

Description of Material

Page(s)   18241-18249

I will acknowledge the original source as specified at the https://rsc.li/permissions.

Signed: Jacob Hunter West   Date: 18 March 2024

The Royal Society of Chemistry hereby grants permission for the use of the material specified above in the work described and in all subsequent editions of the work for distribution throughout the world, in all media including electronic and microfilm. You may use the material in conjunction with computer-based electronic and information retrieval systems, grant permissions for photocopying, reproductions and reprints, translate the material and to publish the translation, and authorise document delivery and abstracting and indexing services. Please note that if the material specified above or any part of it appears with credit or acknowledgement to a third party then you must also secure permission from that third party before reproducing that material. The Royal Society of Chemistry is a signatory to the STM Guidelines on Permissions (available on request).

Signed: *Becky Roberts*
C0B8BD4FBFD54CA...

Date: 19/3/2024 | 12:16 PM GMT

CURRICULUM VITA

Jacob Hunter West, EIT

Louisville, KY
(606) 585-3357
jhwest02@louisville.edu
www.linkedin.com/in/jhwest

EDUCATION

University of Louisville J.B. Speed School of Engineering, Louisville, KY
- Bachelor of Science in Mechanical Engineering (4.0 GPA)   May 2023
- Master of Science in Mechanical Engineering (4.0 GPA)   May 2024

Certifications / Test Scores:
- GRE (Verbal: 162, 90th %ile; Quantitative: 169, 93rd %ile; Writing: 5.0, 91st %ile)   Taken May 28, 2022
- KYBOELS Engineer in Training (Mechanical)   Issued August 2023
- CRLA Certified Master Tutor (Level 3)   Issued December 2022
- IISE Six Sigma Green Belt   Issued October 2020

HONORS / AWARDS

- Frederick N. Andrews Fellowship, Purdue University (2024)
- Graduation with Highest Honors, BSME (2023)
- J.B. Speed School of Engineering Outstanding Student Award (2023)
- Tau Beta Pi KY Beta Chapter Advisor (2024)
- Tau Beta Pi KY Beta President (2023), Vice President (2022)
- J.B. Speed School of Engineering ASME Leadership Award (2023)
- UofL Honors Program Completion (2023)
- ME Department Chair Review Committee (2023)
- UofL ASME Chapter Treasurer (2022)
- UofL ME Department Student Advisory Council (2022)
- J.B. Speed School of Engineering Outstanding Freshman Award (2020)
- KYTSA Board of Directors Secretary (2019-2020)
- U.S. Dept. of Ed. Presidential Scholar (2019)
- NMSC National Merit Scholar (2019)

WORK EXPERIENCE

University of Louisville – Louisville, KY

Graduate Teaching Assistant, Dept. of Eng. Fundamentals *Aug 2023 – May 2024*
- Collaborates with faculty to improve educational materials for courses
- Supports lecturers during class sessions by assisting with class activities
- Holds weekly office hours for students seeking coursework assistance
- Grades submitted assignments and assists in rubric development

Master Tutor Mentor / Peer-assisted Learning Tutor, REACH *May 2021 – May 2023*
- Tutored students in Eng. Fundamentals and Mechanical Eng. courses
- Hosted collaborative learning sessions for Engineering Calculus courses
- Mentored fellow tutors in effective techniques and practices of tutoring

Student Ambassador, Speed School Office of Admissions *Aug 2020 – May 2022*
- Guided tours of engineering school facilities and presented on program
- Staffed admissions recruitment events for prospective eng. students

Student Assistant, Department of Eng. Fundamentals *Jan 2020 – Dec 2020*
- Developed and reviewed gradings rubrics for eng. calculus exams
- Graded exams for Engineering Analysis I & II courses
- Supplied feedback to students upon request of grading clarifications

CMTA Energy Solutions – Louisville, KY

Mechanical Engineering Co-op *(3 rotations totaling 50 weeks) Jan 2021 – Aug 2022*
- Commissioned mechanical equipment controls systems
- Prepared construction drawings, technical reports, and presentations
- Presented to project managers and energy engineers on project tasks
- Performed on-site facility audits and equipment commissioning

RESEARCH EXPERIENCE

Integrated Microfluidic Systems Laboratory   *Jan 2023 – May 2024*
- Designed and fabricated experimental test devices and procedures for characterization of frequency-dependent electrokinetic particle trapping
- Prepared posters and slides for presentation of research results at academic conferences
- Collaborated with faculty advisor and graduate students in experimentation and prototyping

ElectroOptics Research Institute & Nanotechnology Center   *Aug 2022 – May 2023*
- Assisted research investigating viscoelastic polymer stretching instabilities
- Investigated methods of directing local shape shifting of thin-film polymer sheets
- Developed experimental specimens and procedures for data collection and analysis

PUBLICATIONS

JH West, TK Mondal, and SJ Williams, "Electrokinetic particle trapping in microfluidic wells using conductive nanofiber mats," *Electrophoresis* (submitted).

TK Mondal, JH West, and SJ Williams, "An Electrospun Nanofiber Mat as an Electrode for AC-Dielectrophoretic Trapping of Nanoparticles," *Nanoscale*, 2023, DOI: 10.1039/D3NR04496C.

ORAL PRESENTATIONS

JH West, TK Mondal, and SJ Williams, "Electrokinetic micro- and nanoparticle trapping using electrospun conductive nanofiber mats," *76th Annual Meeting of the APS Division of Fluid Dynamics*, Washington, D.C., November 19-21, 2023.

SJ Williams, TK Mondal, and JH West, "Enhanced particle trapping using carbon nanofiber mats," *NNCI Nano + Additive Manufacturing Summit 2023*, Louisville, KY, July 25-26, 2023.

POSTER PRESENTATIONS

JH West, TK Mondal, AVB Bangaru, SJ Williams, "Well-based dielectrophoretic particle trapping experiments using conductive nanofiber mats," *Dielectrophoresis 2024*, Dublin, IRL, July 1-3, 2024 (submitted).

TK Mondal, JH West, and SJ Williams, "Electrospun nanofiber mat as an electrode for dielectrophoretic trapping of nanoparticles," *NNCI Nano + Additive Manufacturing Summit 2023*, Louisville, KY, July 25-26, 2023.

JH West, TK Mondal, and SJ Williams, "Dielectrophoretic trapping of particles using a conductive nanofiber mat," *97th ACS Colloid & Surface Science Symposium*, Raleigh, NC, June 4-7, 2023.